Hannes Vennekate

II. Physikalisches Institut
— Universität Göttingen —

Master Thesis:

Second Sound for Heat Source Localization

by Hannes Vennekate

II.Physik-UniGö-MSc-2011/02

Working Time:	April 1^{st} – September 30^{th}, 2011
Supervisor:	Dr. Michael Uhrmacher
	Dr. Wolfgang Weingarten
First Referee:	Prof. Dr. Arnulf Quadt
Second Referee:	PD Dr. Jörn Große-Knetter

Contents

Abstract

Defects on the surface of superconducting cavities can limit their accelerating gradient by localized heating. This results in a phase transition to the normal conduction state — a quench. A new application, involving Oscillating Superleak Transducers (OST) to locate such quench inducing heat spots on the surface of the cavities, has been developed by D. Hartill et al. at Cornell University in 2008. The OSTs enable the detection of heat transfer via second sound in superfluid helium. This thesis presents new results on the analysis of their signal. Its behavior has been studied for different circumstances at setups at the University of Göttingen and at CERN. New approaches for an automated signal processing have been developed. Furthermore, a first test setup for a single-cell Superconducting Proton Linac (SPL) cavity has been prepared. Recommendations of a better signal retrieving for its operation are presented.

Part I.

Theory

Chapter 1.

Motivation

1.1. Superconducting Cavities

When it comes to particle physics, particle colliders have become the work horse of nearly all "active" experiments — if the focus is not on the observation of astrophysics. The essential components of these machines can in general be divided into two groups, the detector and the accelerator structure — no matter if it is a fixed target or a real "two-beam" collider. While the detector covers the observation of the physical process, the accelerator has to facilitate this process in the first place. The accelerating structure itself again consists of several essential building blocks. Beginning with the initial particle source, the so-called beam line usually features all kinds of magnets — for example dipoles to bend and quadrupoles to focus the beam — and sensors to keep track of the beam's attributes. In order to gain momentum, the particles have to travel through a series of cavities. The fundamental principle of the acceleration here is based upon a standing or traveling electromagnetic wave excited in these cavities. This wave keeps on pushing the particles down the beam line. This is also the reason why only charged particles can be accelerated in these machines. The fundamental process is illustrated in the scheme in figure 1.1.

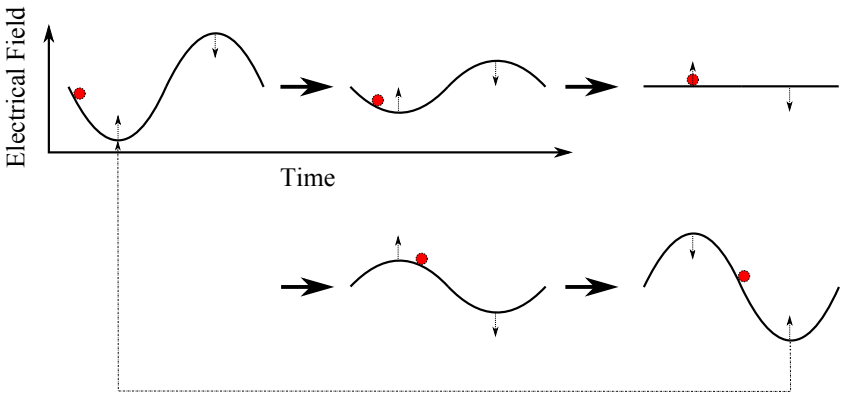

Figure 1.1.: Two dimensional example for particle acceleration with a standing wave.

As the progress of research proceeds, the demand for better particle beam characteristics provided by the accelerator grows. On the one hand higher energies of the individual particles are of high priority while on the other hand further improvements like a high

stability and low emittance of the particle bunches are supposed to be achieved. There are different approaches to fulfill these goals. The topic of this thesis refers mainly to the ones including superconducting (elliptical) cavities.

Two main examples are going to be dealt with as they give the motivation for the described application in cavity quality diagnosis. The first being the nine-cell 1.3 GHz TESLA cavity and the second being the 704 MHz SPL with five cells per cavity. To put the particular meaning of this work into the appropriate context, a short description of these two concepts and the corresponding projects shall be given in the following:

TESLA — A new Cavity Standard

The TeV-Energy Superconducting Linear Accelerator (TESLA) was a project for a linear electron-positron collider, including a free electron laser, in Germany. Although the project did not get sufficient funding for a full realization, its accelerator concept — basically the cavity design — has defined a new standard for a couple of other projects. One being the future ILC concept (International Linear Collider) which is supposed to be a linear accelerator with a length of over 30 km colliding electrons and positrons at energies of 500 to 1000 GeV.

Figure 1.2.: A TESLA cavity made out of pure Niobium, from [1].

The motivation for this machine is to become the corresponding tool for high precision measurements of any new physics that might be discovered at the currently running LHC (Large Hadron Collider). This includes the Higgs boson, any supersymmetric particles or the mass of the already discovered top quark and the W and Z bosons [2]. The needs of this project in terms of accelerator components are respectively high, a total number of well above 15000 TESLA cavities that run at a field gradient of at last 31.5 MV/m [3] . One of the current projects with the same cavity design, which is already in its construction phase, is the European Xray Free Electron Laser (XFEL) at DESY, Hamburg. This 3.4 km long apparatus is supposed to fire high energy electrons (17.5 GeV) through an undulator[1], causing them to radiate high intensity bright laser light which can be used for all kinds of other scientific projects. Since this machine makes it possible to create light flashes with a duration of less then 100 fs, fast chemical reactions for example can be examined much better than ever before. From the accelerator physics

[1] An undulator forces the electron bunches to oscillate back and forth via an alternating magnetic field so that they radiate photons of a certain wave length.

point of view this project needs much less cavities than the ILC, but still in the order of 1000 which are supposed to reach field gradients of 23.6 MV/m [4]. A smaller version of the XFEL, the FLASH, Free Electron Laser in Hamburg, is already in use. It originates of the former TESLA test facility and operates seven 1.3 GHz modules — besides a new 3.9 GHz module — at different gradients. It serves both, test and already productive purposes.

SPL — Superconducting Proton Linac for the LHC

The second example for superconducting accelerator technology is the SPL study at CERN. This study has also been the framework for the final experiments of the presented thesis. Furthermore some of the related projects, which were started with this work, will also be continued in the near future.

SPL stands for Superconducting Proton Linac (i.e. linear accelerator) and was a project first thought of in the late 90s at CERN. The early concept of '99 was to use rf (radio frequency) equipment of the dismantled Large Electron Positron collider (LEP) accelerator to build a new superconducting linac at the energy of 2.2 GeV in order to replace the old Linac2 and the Booster and directly inject into the Proton Synchrotron (PS). This concept would cause a number of advantages over the current setup — at least at the first stage of the proposal — at the low cost of using decommissioned parts from LEP. The SPL would upgrade the existing injector chain of the LHC (Large Hadron Collider) and provide much better beam characteristics. At the same time it would have spare energy for other clients as well. It was for example thought to be used as a beam supply for a future neutrino factory and as a possible low power proton source for radioactive ion beams for a future version of the On-Line Isotope Mass Separator ISOLDE [5].

The latest concept includes the separated normal conducting Linac4 as an injector for the SPL itself. As this accelerator is supposed to deliver a beam at 160 MeV it is a suitable replacement and upgrade of the existing Linac2 on its own and could directly inject into the Booster followed by the PS. In the framework of the SPL scheme this linac will transfer the beam to the superconducting structure, the SPL itself will then inject its beam into a new Proton Synchrotron (PS2) which is still to be built. The new concept features completely different cavities for this version of the SPL, as shown in figure 1.3. The frequency for these has been changed to 704 MHz as new parameters for the elliptical, now five-cell cavities have been worked out. The architecture of the whole beam line consists of a first stage for particles at a β of 0.65 and a longer second part serving particles at a $\beta \approx 1$.[1] To this track several extraction points for transfer lines to different clients may be added. The proposed layout with the highest final energy sets this at 5 GeV.

[1] β is the ratio of the velocity of the particles to the velocity of light in vacuum.

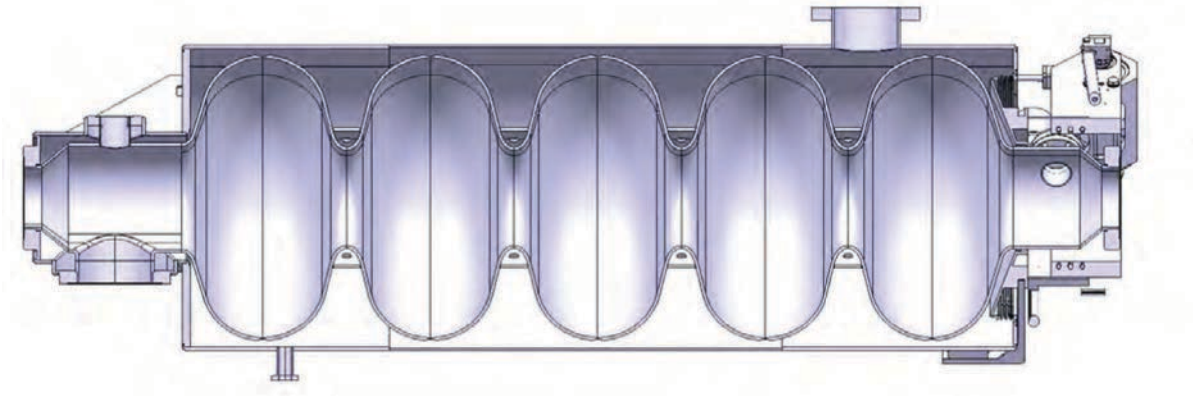

Figure 1.3.: Proposal of the superconducting five-cell SPL cavity in its cryostat, from [6].

Looking at the relevant numbers for the cavity installation, the $\beta = 0.65$ part is designed to work with 60 cavities at a field gradient of 19 MV/m, while the $\beta = 1$ section needs 184 cavities with a stable field gradient of 25 MV/m [6, 9].

In summary, there are all kinds of efforts in the field of superconducting rf cavities which all have in common, no matter if it is for a collider, free electron laser or injector, that a relatively large number of cavities — at least in the order of 100 — is supposed to work in stable operation at high field gradients. And as the injector represents the backbone of the whole accelerator chain, since it is responsible for the initial transverse and longitudinal emittance, the linac in a free electron laser is the tool to unleash its full potential and the performance of each accelerating module in a collider is vital to the energy at its point of intersection. So the reliability of each individual cavity is of significant importance to the whole experiment independent from the form of application. This makes severe quality diagnosis mandatory as well as a sophisticated understanding of the limiting factors for the deployability of the structures.

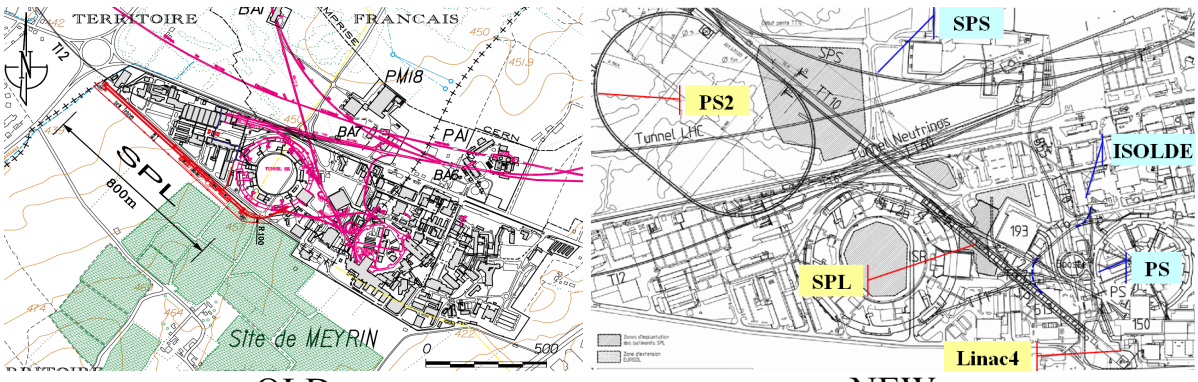

OLD NEW

Figure 1.4.: Not only frequency and energy of the proposal have changed — the favored position on the CERN site has changed too. See [7, 8] in comparison.

1.2. Why Superconductivity and what are the Limits

Superconductivity has been of particular importance for quite some time now when it comes to modern particle accelerators. While superconducting (sc) magnets have become more or less irreplaceable especially in circular hadron machines — not to mention that there are no alternatives to superconducting cables to supply the extreme high currents to them — superconducting cavities are not the only option to gain high energy particle beams. Nevertheless this technology dominates the majority of design efforts for particle acceleration in the near future. To understand this situation, the advantages mainly in comparison to normal conducting approaches are summarized in the following.

The main advantage of a superconductor over a normal conducting material is its zero resistivity when it comes to transferring any current. For radio frequency sc cavities used for particle accelerators this is actually not true. Skipping the details of the BCS[1] theory for superconductivity, it is a known fact that superconductors get a quantifiable resistivity for alternating currents as created in a radio frequency field. This is caused by free electrons not being bound in bosonic Cooper pairs and their resistive response to the voltage created by the Cooper pairs in the alternating field, for more details see [10, 11, 12]. The resistance is proportional to the square of the frequency, $R_s \sim \omega^2$, as well as it is linked to the temperature, which regulates the number of non-bound electrons, $R_s \sim \mathrm{e}^{-\frac{1}{\mathrm{T}}}$, see [11] for a derivation.

Despite this behavior, the actual values of this resistivity are still relatively small — for niobium, which is widely used for rf sc cavities, usually in the order of a few nΩ — conserving the advantage over any normal conducting material. However, this benefit has to be paid for with the low temperatures that have to be obtained during operation. A good cooling is always necessary however expensive. In a normal setup this means that the cavities are installed inside big cryostat vessels, filled with liquid helium at temperatures below at least 5 K.[2] Though relatively complex, these systems guarantee an efficient cooling that in combination with the very low losses due to the small surface resistance of the cavity makes it possible to operate the whole structure in continuous wave mode. Reaching for such high energies, normal conducting accelerator structures are often only able to run in pulsed mode. The cooling of their cavities — in most cases made of copper — gets harder due to the dramatically increasing ohmic heating. In general, the share of the supplied electrical power that gets transferred to the particle beam is much bigger in a superconducting accelerator than in a normal conducting one.

At the same time there are further advantages linked to the very high quality factors Q_0[3] of sc cavities. These enable for example the implementation of bigger apertures in the beam line design, reducing unwanted beam-cavity interactions. Though the Q_0

[1] Bardeen-Cooper-Schrieffer

[2] The cavities of LHC are for example cooled down to 4.5 K which means that the liquid helium is above atmospheric pressure.

[3] Stored Energy divided by power dissipation per cycle times the circular frequency or the number of oscillations until the stored energy dropped down to 1/e — for contemporary niobium cavities values of 10^{10} or 10^{11} for Q_0 can be achieved [13].

suffers from these bigger diameters of the cavities irises, the initial values are usually big enough to allow this enhancement while quality factors of normal conducting cells do not.

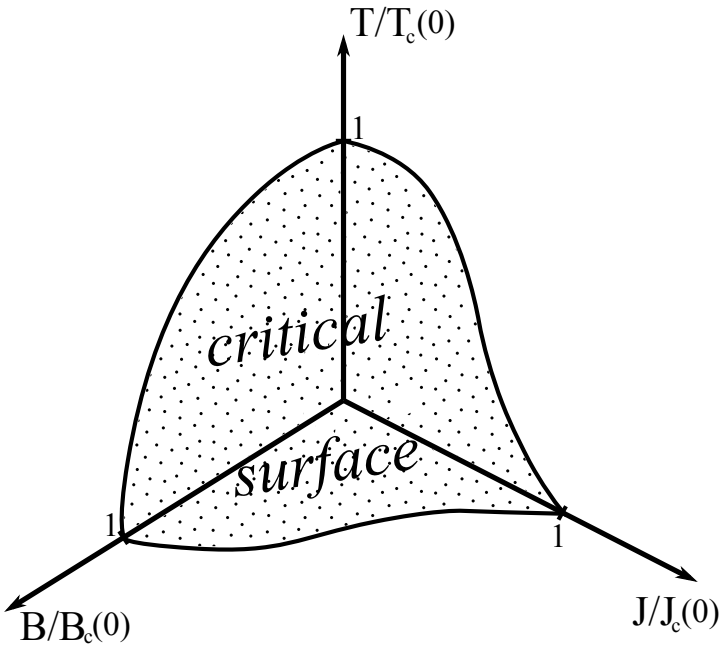

Figure 1.5.: The critical surface of a superconductor: In the region below the indicated surface of the applied B-field, transport current J and temperature T the material stays in its superconducting state, refers to [10].

Despite all these advantages there are also limitations to the application of superconducting cavities. The extensive efforts to keep the material at very low temperatures have already been mentioned. In addition to that, the magnetic field, which is a function of the electrical field used to accelerate the charged particles, may also cause the deployed material to leave its superconducting state. The reason for this in the framework of the BCS theory is the circumstance, that the Cooper pairs, being responsible for the resistance free current transfer, try to expel any external magnetic field. As they do so, they gain in energy, reach the level of normal conducting free electrons — at a certain critical field B_c — and the superconductivity is lost.[1] These boundaries give a three dimensional volume as depicted in figure 1.5 with a critical surface that limits the conditions for the preferable sc state. As the energies of the particle beams in new experiments are demanded to reach higher and higher levels, the field gradient inside the cavity's cells has to be increased in order to keep the length of the whole accelerator within feasible dimensions. At the same time a decrease in temperature in the cooling system presents itself as being quite costly as well. Finally a compromise has to be achieved not only for financial but also for reasons of stability in operation of the structure. The prediction for the theoretical limit on the field gradient in niobium cavities is in the order of 55 to 60 MV/m. These gradients are barely reached with special single-cell designs[2] while the actually tested cavities with a multi-cell design have maximum gradients of 25 to 45 MV/m [15]. Due to impurities and imperfections in the bulk material caused by the manufacturing process, the limiting boundaries are attained earlier at these individual weak spots provoking the whole system to fail. This event is referred to as a "quench" of the cavity and it works like a chain reaction. The "seed" of the quench, if being a surface irregularity, faces a higher electric or corresponding magnetic field as the rest of the

[1] According to [11] the B_c is about 200 mT for pure niobium.
[2] At Cornell University a world record gradient of 59 MV/m was reached [14].

superconducting surface. If being a normal conducting inclusion, its direct environment develops exceptional heating. At some point it breaks through the critical surface and becomes normal conducting. From that time on it generates a lot of heat as it is still part of the whole conductor transferring high currents. In an avalanche the surrounding areas lose their superconductivity as they warm up likewise. The result is, that the complete cavity quenches and the injected energy cannot be transferred anymore. In order to understand these restraints of the technology and to deal with them in a better way, the localization and examination of exactly these quench spots is of great interest.

1.3. Temperature Mapping

One way to locate the heat sources resulting in a quench used in laboratories around the world is the temperature mapping (T-Map) technique. It is based on small resistors which, mounted close to the surface of the cavity, change their resistivity in case of small changes in temperature in the liquid helium.

There are different conceptual designs for the positioning of these sensors. In principle they can be divided into the two main options of fixed and moving arm design. A fixed installation, as shown in figure 1.6, requires a much bigger number of resistors while the results of the measurement are obtained in a rather short time interval. Moving or rotating arm designs are usually more flexible and can more easily be combined with other sensors like X-ray scanners consuming more time for a measurement. Nevertheless both approaches have to be attached as close to the cavity's surface as possible, before it can be put into a vertical cryostat for the very test measurement. This may get highly complicated as the density of the resistors on the surface affects the spatial resolution of the temperature map later on, making a tight positioning preferable. In summary these difficulties cause a time consuming start-up phase. And besides that, the analysis of a more sophisticated multi-cell cavity design may even require several cooling cycles using a lot of liquid helium and again time.

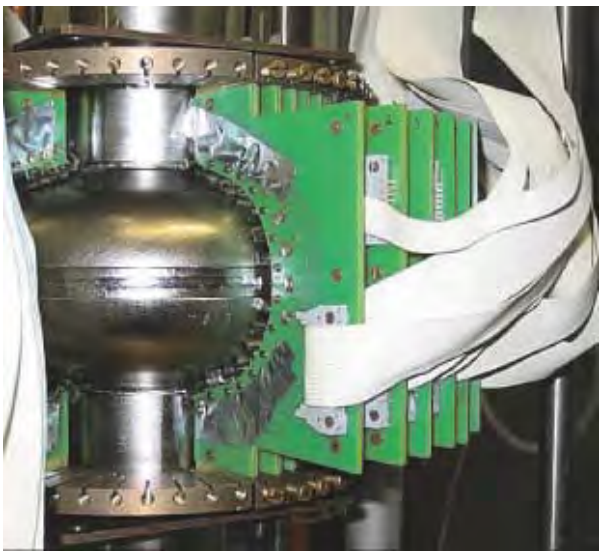

Figure 1.6.: Example of a fixed single-cell T-Map installation at DESY, from [16].

The spatial resolution obtained with contemporary systems is in the order of one or two centimeters depending on the individual setup [11, 16]. As mentioned earlier, this depends mostly on how close the resistors including their wire connections can be placed next to each other, which varies for the different cell regions. In addition to that

the liquid helium, which cools the structure, tends to reduce the maximum theoretical resolvable temperature rise by 20 to 30 % [11].

The result however, may justify all these inconveniences as it provides a reliable information — the temperature map — about the surface's behavior while high power loads are fed into the cavity. Still, one can easily guess that a new solution or new technique in gaining information about the heat activity on the cavity would be worthwhile. Especially a solution that does not require a direct installation on the cells themselves and reduces the number of needed cooling cycles. This leads to the topic of this thesis as the application of second sound sensitive devices might fulfill these systematic prerequisites. Nevertheless, the advantage of temperature mapping lies in its capability to detect predecessors of quench spots and their dependence on the magnetic field while second sound can only be used to detect the spot itself.

Chapter 2.

Cavity Diagnostics with Second Sound

2.1. Two Fluid Model of Superconductivity

The effect of second sound gained its name from the circumstance that it represents a sound like wave propagation of heat in superfluid states. The phenomenon is best understood in the two fluid model developed by Laszlo Tisza, which is roughly explained in the following.

When liquid helium is cooled down, it performs a phase transition at 2.17 K [12], the λ-point. The name is taken from the characteristic behavior of the specific heat capacity as shown in figure 2.1. For an easier distinction, the phase below this point is referred to as "helium II". As soon as liquid helium reaches these temperatures, special phenomena can be observed, like the almost instantaneous end of bubble formation caused by the large thermal conductivity of the fluid. Further attributes of the liquid suggest that it becomes superfluid, while other observations show that it still bears a viscosity. Motivated by an idea of Fritz London, who unveiled parallels of helium II to a Bose-Einstein condensate, Laszlo Tisza created a two fluid model to cover both observed criterion. The model can be explained like this: When reaching the λ-point, a fraction of the helium atoms condenses into one shared, lowest energy state, forming a superfluid liquid. The rest of the helium atoms keeps its normal fluidity and coexists with the other. As shown in figure 2.2, the superfluid fraction becomes more and more dominating with decreasing temperature until the normal fluid helium vanishes for very low temperatures. As the whole "body" of helium has to be considered as a

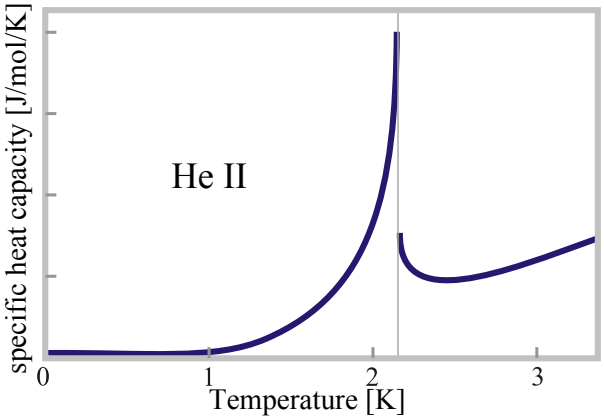

Figure 2.1.: Scheme of the specific heat capacity of liquid helium as a function of temperature around the λ-point, the shape of the curve giving this special name. Compare [12].

mixture of the two components, the total density is given by the sum of the individual ones:

$$\rho = \rho_s + \rho_n$$

ρ_s giving the density of the superfluid fraction, while ρ_n is the one of the normal fluid fraction.

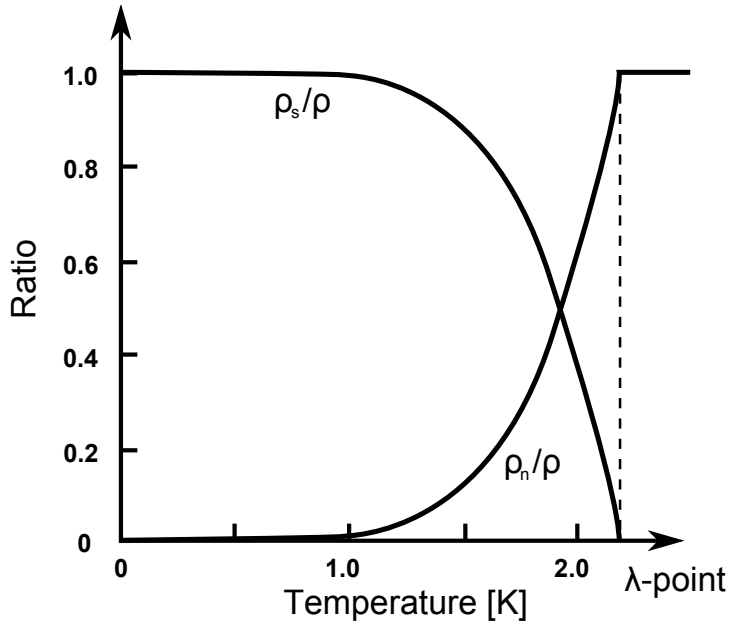

Figure 2.2.: Relative densities of superfluid and normal fluid versus temperature below the λ-point in helium.

In order to explain the different behaviors, the two fractions consequently differ from each other in their physical attributes. By definition the viscosity of the superfluid component equals zero, furthermore it bears no entropy, whereas the normal fluid fraction has still a non-zero viscosity and keeps the total entropy of the composite. Adding individual velocities to the fractions, results in two equations of motion as described in [17] leading to two wave equations with independent propagation velocities. One of them is commonly known as "first" sound. It describes the longitudinal fluctuation in density which is driven by pressure variations as illustrated in the upper part of figure 2.3, taken from [18].

The other wave equation represents what was named "second sound" by the Russian physicist Lev Landau and describes a fluctuation in entropy driven by temperature — shown in the bottom part of figure 2.3. The resulting heat transfer works essentially as a counterflow of the superfluid and normal fluid fraction of the liquid. So when heat is generated at a spot in the helium II, a surplus of normal fluid is created. It generates a wave that propagates in all directions away from this source. Hence, wavefronts of superfluid helium move in the opposite direction to compensate the disturbance of the equilibrium.

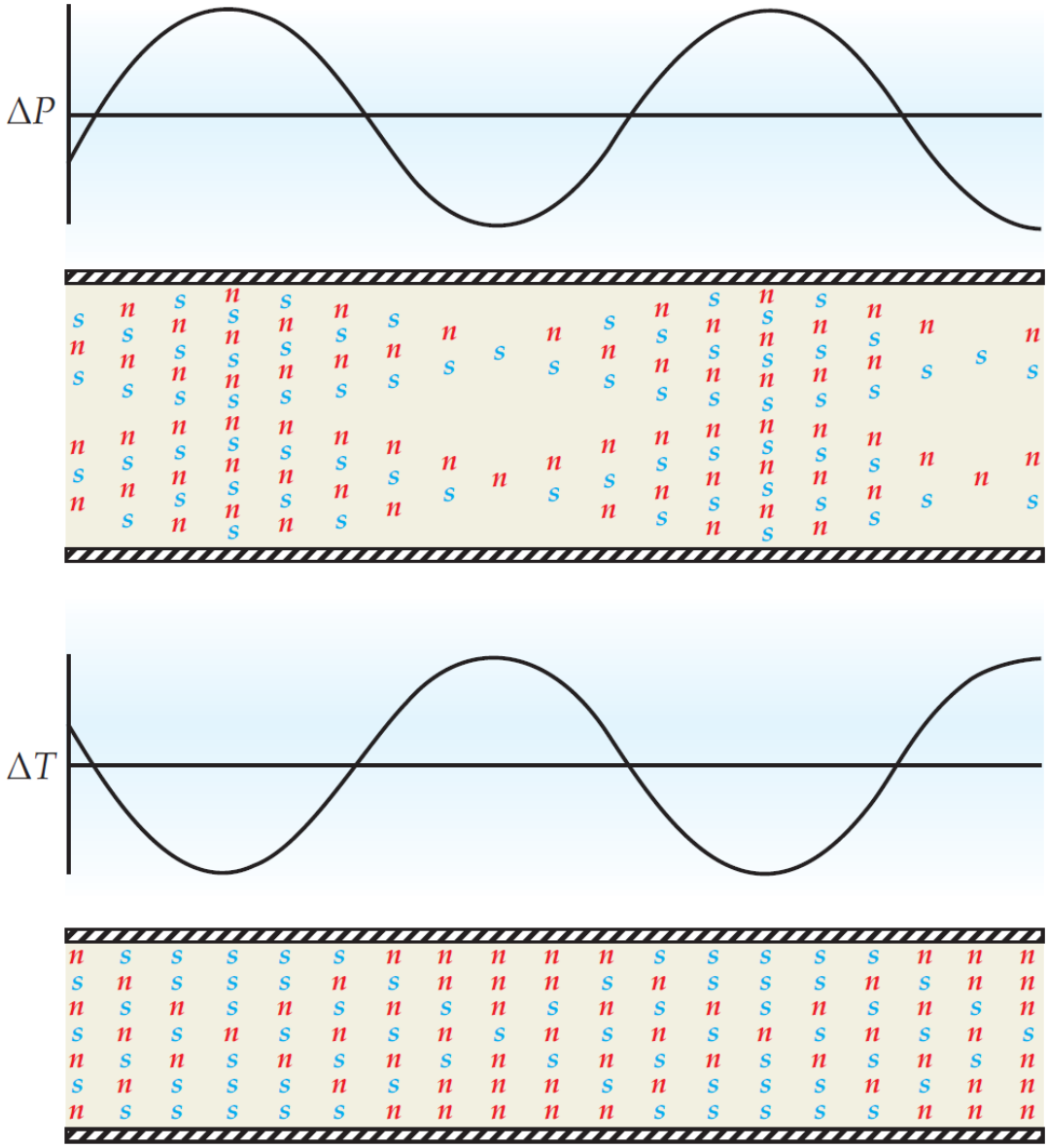

Figure 2.3.: The ratio of the letters n and s in every vertical column represents the relative portion of the superfluid and normal fluid helium while the total number of symbols corresponds to the density of the mixture. The upper part of the scheme illustrates first, the lower second sound, see [18] for more details.

2.2. Oscillating Superleak Transducers

Back to superconducting rf cavities, the situation of a (vertical) test stand presents itself like this: The cavity is mounted in a cryostat and kept at very low temperatures with liquid helium. An antenna feeds the rf power into the resonator to establish a resonance of the electromagnetic field. At a certain field strength, the cavity might quench, disrupting the power transfer. In the case, a single spot on the surface of one of

the cells is responsible for this failure, its position might be determined using temperature mapping and the moment the transferred signal is lost as a trigger as described above. Yet, as the hypothetical weak spot on the surface heats up when turning back into its normal conducting state, it will also generate a second sound wave in the coolant, provided that its temperature is below the λ-point. If this entropy wave can be detected from different points of view in the cryostat — by spatial distributed detectors —, a localization of the initial seed is possible.[1]

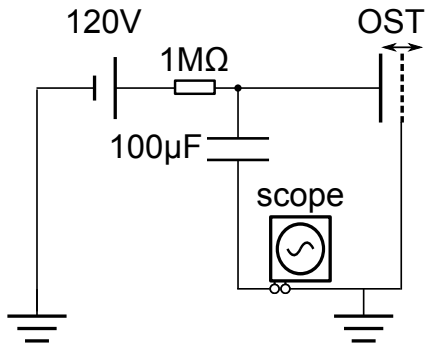

Figure 2.4.: Simplified OST readout and power supply circuit as used in Göttingen, compare figure 2.4 and 3.1.

But how can the phenomenon of second sound be observed in a quantitative manner? The answer to this question is a sensor called "Oscillating Superleak Transducer". This detector is basically a plate capacitor with a fixed and a flexible electrode. The latter has to be "superleak", which means that it is supposed to let superfluid helium pass through while normal fluid is kept out. This capacitor is placed in an electrical circuit like in figure 2.4, becoming very similar to a capacitor microphone. This has the reason that it serves as just the same — a "microphone" for the second sound. The sequence of events during a measurement of the same is listed below:

1. The OST capacitor is charged by an external current source inside the liquid helium II, the source being outside. It bears the charge of

$$Q = C \cdot U, \tag{2.1}$$

   with C its capacity and the applied voltage U.

2. A heat source (the quench spot) creates a second sound wave — a surplus of normal fluid helium travels away from the hot spot, towards the OST.

3. The normal fluid wavefront hits the "superleak" capacitor plate. As it cannot pass through, it pushes the conducting gold layer closer to the second, fixed electrode.

4. Because of the resistor which is in series to the capacitor, the charge on the OST's plates is kept constant for short time intervals:

$$\begin{aligned} & \frac{\mathrm{d}Q}{\mathrm{d}t} = 0 \\ \Rightarrow \qquad & \frac{\mathrm{d}U}{U} = -\frac{\mathrm{d}C}{C} \end{aligned}$$

[1] This method has been introduced recently (2008) by D. Hartill et al. at Cornell University [19], but there were similar ideas and applications developed in the past [20].

As the capacity is proportional to the area of the plates divided by the distance between them,

$$C \sim \frac{A}{d}$$

the capacity increases, when the normal fluid helium hits the sensitive side of the device, causing the voltage to drop:

$$d \downarrow \quad \Rightarrow \quad C \uparrow \quad \Rightarrow \quad U \downarrow$$

5. In the readout system — so on the oscilloscope indicated in figure 2.4. — a decrease in the voltage is registered. Since the flexible plate of the capacitor will return into its initial position after a certain number of oscillations, corresponding oscillations of the voltage signal can be observed.

An example of such a signal triggered by an artificial heat pulse is presented in figure 2.5. If the temperature of the helium is known, one can use the time of flight in combination with the known second sound velocity and compute the distance between heat source and OST.

The OST concept has been realized inside a cylindrical aluminum casing — a two dimensional cross section is shown in figure 2.6. The fixed capacitor plate is a brass electrode that is glued into the backside of the casing and connected to the core of a shielded plug on the exterior. A polycarbonate circular membrane with a diameter of 25 mm and pores of a diameter of 0.2 µm ("Nuclepore Polycarbonate" membrane produced by the company WHATMAN) plays the part of the superleak and flexible plate. It is made conductive on the side that does not directly face the other electrode, by sputtering a gold layer of 50 nm on it. Its flexibility is granted by an aluminum ring that connects it to the rest of the casing.[1] The ring has an inner diameter of 19 mm while the sputtered region on the membrane is slightly bigger than that. Therefore, the gold layer is connected via the aluminum ring and via the rest of the casing to the shield of the backside plug. The voltage, used to charge this capacitor, is about 120 V for the described experiments, the resistivity, mentioned for the circuit, is in the order of 1 MΩ. The OSTs themselves, used during the measurements, were all produced at Cornell University, DESY or CERN — the membranes from Cornell have an aluminum layer as well, but were never used in the experiments at CERN or Göttingen described in this thesis — with the more or less identical design originated from the first draft from 2008.

[1] Compare figure 9.1 in the appendix

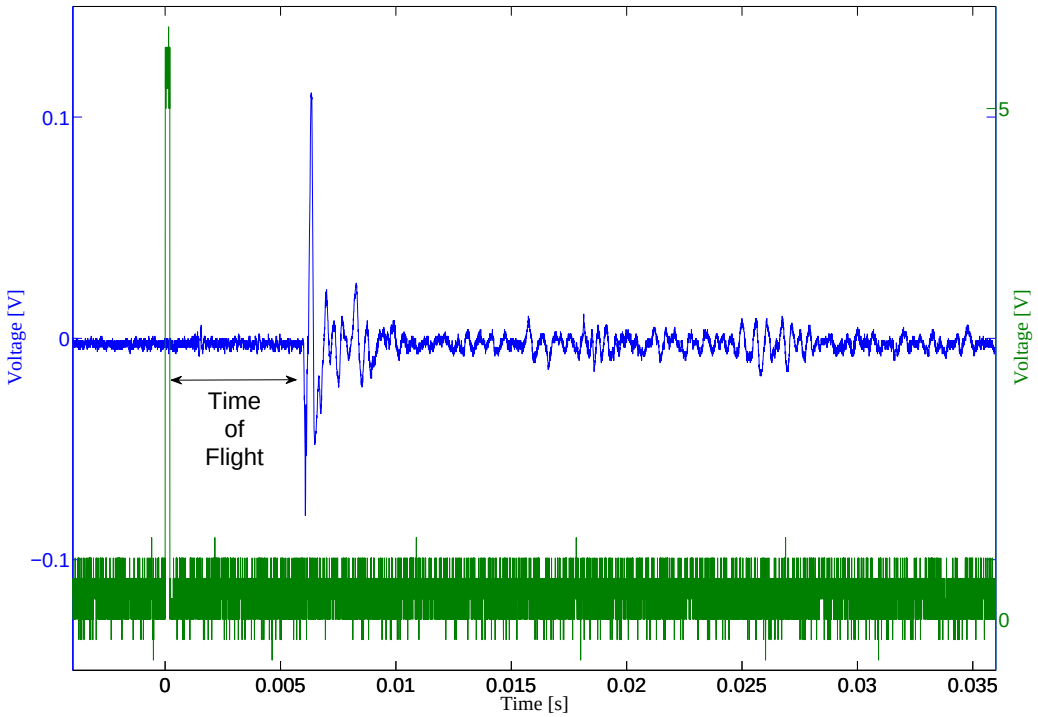

Figure 2.5.: An example for a second sound signal: The green curve with its y-axis on the right represents the heat pulse, while the blue line shows the recorded signal from the OST. The point of interest, as indicated, is the time of flight between the peaks giving the distance between heat source and OST.

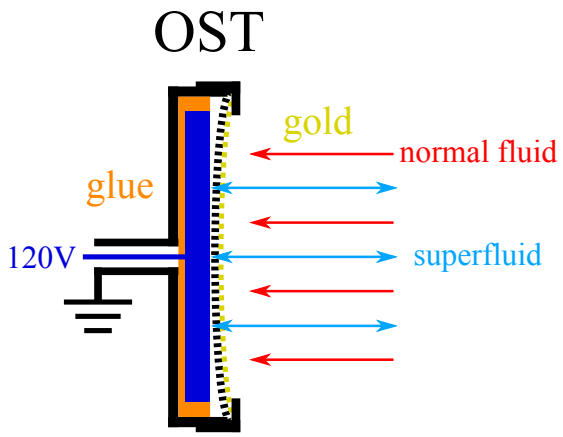

Figure 2.6.: Sketch of the fundamental design of an OST as developed at Cornell University, the brass electrode (blue) is surrounded by insulating glue (orange), while the nonconducting membrane (black) has a 50 nm gold layer on its forefront, compare figure 9.1 for a picture of a disassembled OST, further pictures of the OST manufacturing can be found in the appendix too.

Chapter 3.

Experimental Setups

3.1. Test Setup at Göttingen

The setup in Göttingen, as described in [21] and [22], consists basically of a two-section glass cryostat, the inner being sealed and keeping the liquid helium, the outer containing liquid nitrogen and therefore serving as a heat shield. Hence, the temperature of the helium is controlled via the vapor pressure above the fluid using a rotary vacuum pump using the calibration given in [23]. The pressure is measured with a normal and a logarithmic manometer during the experiments. The error of the second device is in the order of 1 mbar [24]. Inside the helium, a small Surface Mount Device (SMD) resistor with a resistivity of about 90 Ω below 2 K is mounted on a polyvinyl chloride (PVC) platform at the bottom of the glass tube. For symmetry reasons, this platform is connected via three niobium wires, two of these connecting the resistor to an external function generator. The readout and supply circuit, which is depicted in figure 3.1, is based upon the described capacitor microphone principle. The oscilloscope used for the signal recording is a 1 GHz Tektronix $DPO4014$.[1] Mounted on a metal rod in the helium, the OST itself can be moved vertically during the measurements. In order to suppress the unwanted noise in the OST's signal, several modifications to the setup, which was built by Benjamin Schröder for his Bachelor thesis in 2010, have been applied. Their effect on the data will be briefly discussed in part II of this thesis, a more detailed discussion can be found in [22]. The alterations are highlighted in figure 3.1, they include:

1. A series of batteries as the power supply of the OST, having a total voltage of 120 V, which replaced the normal power supply,
2. a new oscilloscope — the mentioned $DPO4014$ — that does not intrinsically suppress noise but has a much higher resolution and smaller device error than its predecessor,
3. a metal box shielding the electronics,
4. the insulation of the BNC cable connecting the OST from the hollow metal rod which holds the sensor,

[1] For the device errors and further information compare [25].

5. a change in the measuring procedure as the rotary vacuum pump is always to be switched off during data taking.

As noted above, the resistor, representing the quench spot and therefore generating the second sound wave, has a resistivity of about 90 Ω at the investigated temperature of 1.5 to 1.8 K — which corresponds to an adjusted vapor pressure of 5 to 16 mbar. The pulse itself lasts 0.2 ms and has an amplitude of 4 V. It is simultaneously recorded on one channel of the oscilloscope to trigger the data taking as shown in figure 3.1.

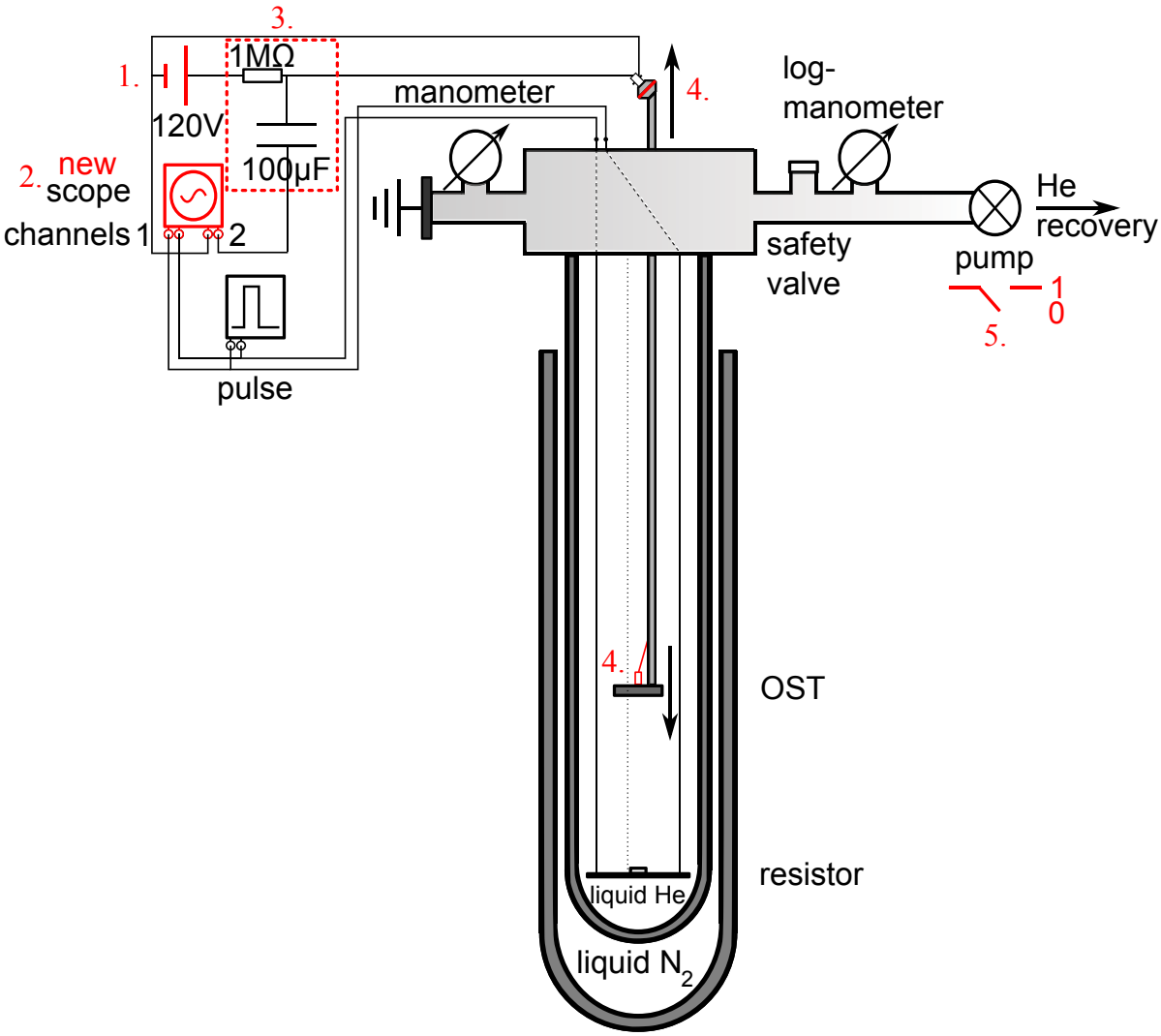

Figure 3.1.: Schematic layout of the glass cryostat and electronic circuit in Göttingen: All the improvements regarding noise suppression and upgrades to the original one of 2010 are indicated in red [22].

3.2. Test Setup at the Cryolab at CERN

The existing setup at the Cryolab at CERN is different in several aspects from the one at Göttingen. The most important difference of it is the diameter of the cryostat which is about 19.5 cm as shown in figure 3.2, whereas the inner glass tube of the cryostat in Göttingen has a diameter of only 7 cm. This allows for multi-OST installations at CERN. Furthermore a stainless steel vessel instead of a glass one is used. The experiment itself is set up on a removable insert. The outer casing has 2 mm thick steel walls, three copper and various aluminum multilayer foil heat shields, which are encased in an evacuated volume around the inner chamber. This results in a better shielding of the sensitive electronic devices. The insert has three copper heat shields directly under its sealing steel cover, which are at the height of the three heat shields in the outer container when the cryostat is closed. At the bottom, another copper plate is installed. It is fixed by three stainless steel rods forming the "skeleton" of the whole structure. The plate is about 10 cm above the vessel's inner bottom when fully inserted. On it a Cernox temperature sensor is fixed, used to determine the temperature of the liquid helium during the experiments. According to its data sheet [26], it has a calibration error of 4 mK below 10 K. Additionally to the Cernox, up to three small boards with SMD resistors have been installed on this plate and were connected to sockets on top of the steel cover of the insert.

The two most used resistors are thick film resistors of the NRC series from the NIC Components Corporation with a face value of 51 Ω and a power rating of 1/8 respectively 1/10 W. Their resistivity below 2 K was measured to be around $62 - 64\,\Omega$ and $65 - 67\,\Omega$. Just like at the setup at Göttingen, these heat sources are connected to an external function generator[1], providing pulses of a length of 0.2 ms and an amplitude of up to 10 V.

The sensors at this setup can be mounted on the three metal rods of the framework as well as on a fourth one which is vertically adjustable during the measurements. The SMD boards on the bottom plate can be placed directly under each OST position during the preparation phase, to simplify the distance determination.

The readout and power supply is in its basic idea very similar to the system at Göttingen, although more complex in design. The power supply is done with a set of batteries, too, in order to avoid any further noise on the signal. Additionally to the basic concept, an amplifier circuit, copied from the original design from Cornell University, is included — see figure 3.3. For the described measurements an amplifier box[2], that contains eight channels – so eight of these circuits —, has been used. The box was built during the summer student program of Karol Krizka at CERN, therefore a detailed description of its functionality can be found in his report [27].

[1] In this case copper cables were used.
[2] Figure 9.2 in the appendix.

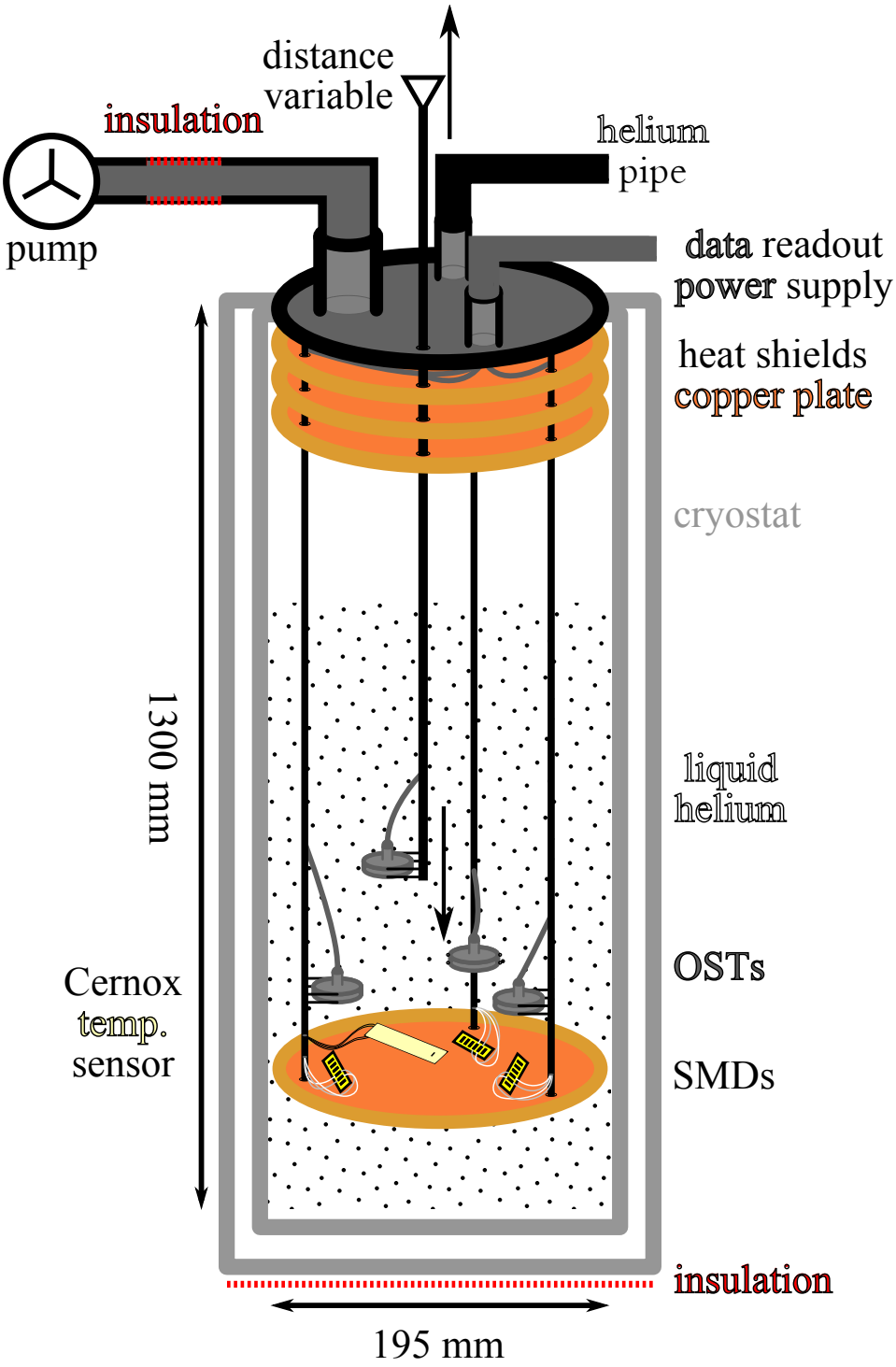

Figure 3.2.: Schematic layout of the metal cryostat used at CERN: The removable insert in this scheme contains four OSTs at all possible installation points — the three supports and the additional adjustable rod. The number of actually installed OSTs varies between the individual experiments. During any measurement, the SMD boards as well as the CERNOX temperature sensor are fixed to the bottom copper plate of the insert. The two highlighted insulation upgrades were installed after May 18^{th} and are shown in figure 9.5 and 9.6.

The important aspect is the provided non-inverting amplification via the included OpAmp-IC of [28]:

$$\begin{aligned}\frac{U_{out}}{U_{in}} &= 1 + \frac{R_1}{R_2} \\ &= 1 + \frac{470\,\mathrm{k\Omega}}{20\,\mathrm{k\Omega}} \\ &= 24.5\end{aligned}$$

Two different oscilloscopes were used for the data taking and first evaluation during the measurements that will be referred to later on. The systematical errors have been adopted accordingly. At first a TEKTRONIX $TDS3014C$[1] was used as it is a battery driven oscilloscope and it was assumed that this may decrease the noise of the OST's signal. As it was shown, that the battery operation mode does not result in any improvement and some device errors during the data storing routine occurred, the oscilloscope was replaced with a newer version — the TEKTRONIX $DPO3014$.[2]

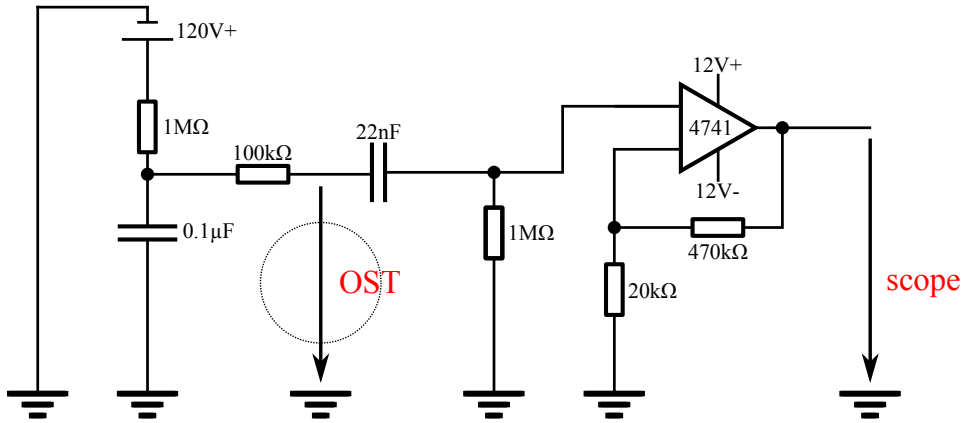

Figure 3.3.: Circuit diagram of the amplifier used in the Cryolab: The 120 V are provided by a set of batteries. The amplification factor of the non-inverting operation amplifier equals 24.5. During measurements, a metal box containing eight of these circuits and the batteries for the power supply, has been used, see figure 9.2 for a picture. For more details see [27].

After first measurements, modifications to the setup became necessary to disconnect the Cryolab's ground from the system. Corresponding pictures of the installations can be found in the appendix.

The rotary vacuum pump[3], used to lower the vapor pressure above the liquid helium, is connected to the cryostat via a long and extensive system of pipes and valves.

[1] For a manual see [29].
[2] For a manual see [30].
[3] Rotary vane pump 100 $\mathrm{m^3/h}$.

Part II.

Results

Chapter 4.

Results Göttingen

4.1. Noise Suppression

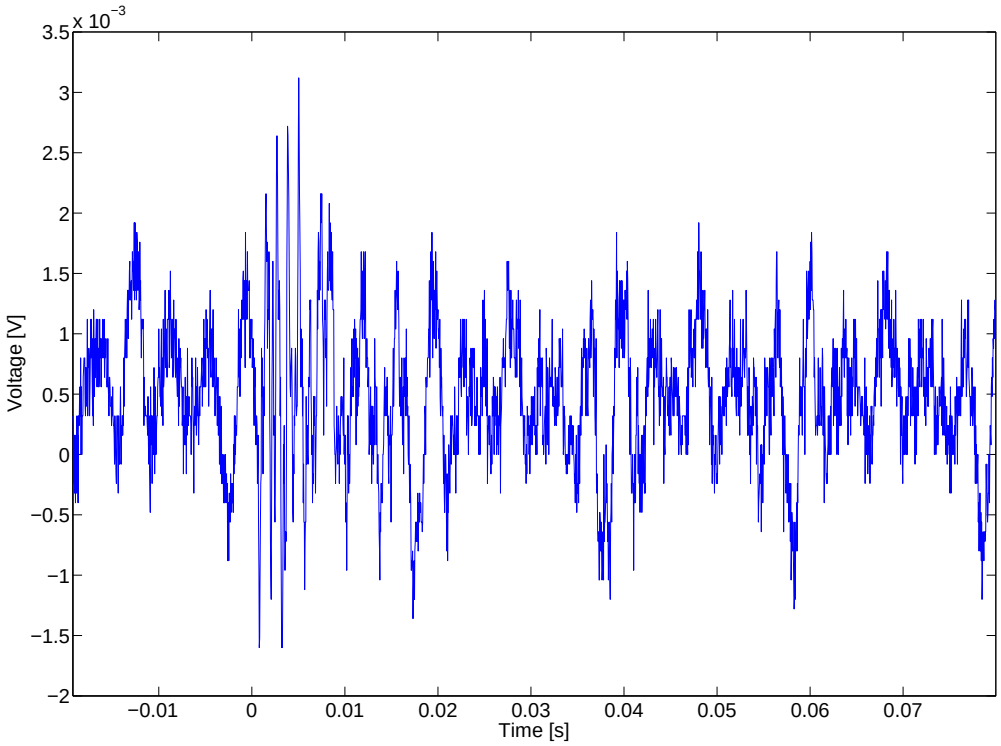

Figure 4.1.: Second sound signal measured on July 26^{th}, 2010 at $\approx 1.4 - 1.5\,\text{K}$, based on the old setup before noise improvements were added, see [21].

The main task at the beginning of the measurements in Göttingen was to suppress the immense noise background in the OST's signal, since it was very hard to resolve the actual second sound signal as the data presented in figure 4.1 shows — the signal starts

shortly after the trigger at 0 s. The analysis of the noise has shown that its frequency is in the regime of 50 Hz and higher harmonic modes of that, up to about 300 Hz [21, 22].

Because of that, especially the power grid and the vacuum pump were candidates for the origin of this background as they both operate at 50 Hz. As listed in the description of the setup in Göttingen, the system has been modified to fight these effects. Except for the oscilloscope itself, the circuits were separated from the grid by replacing the power supply with a series of batteries and installing several insulations. Furthermore, the capacitor microphone circuit has been shielded with a metal casing. However, the biggest improvement was achieved by stopping the vacuum pump during the data taking. The pump itself is positioned less than a meter away from the cryostat and connected to its steel cover with bellows. These start vibrating when the machine is in operation and transfer their oscillations to the cryostat. In figure 4.2 an OST signal recorded in the helium without any heat excitation and just the pump running is shown. In the lower part of the same figure, a transformation into the Fourier space proves the domination of the 50 Hz frequency as observed in the recorded signals before.

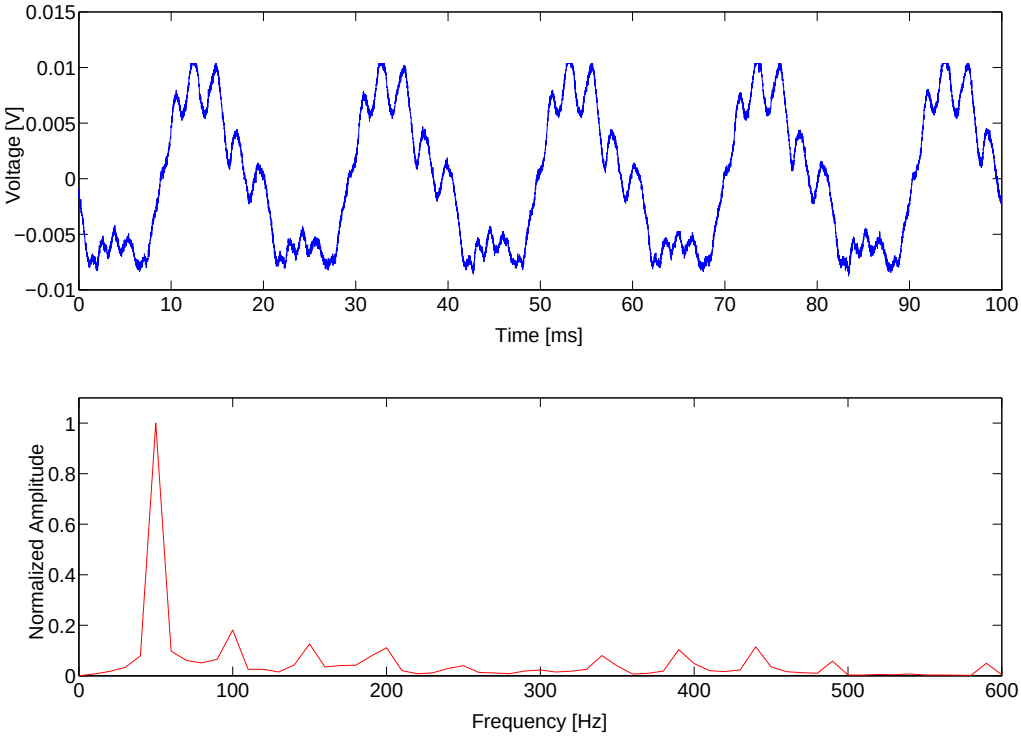

Figure 4.2.: Fourier transformation of the OST noise in superfluid helium with the rotary pump running and no second sound signal.

The result of a second measurement, that demonstrates how the termination of the pump's operation affects the sensor output, is presented in figure 4.3. In less than a

minute all obstructive oscillations are gone. But once the pump is turned off, the vapor pressure inside the cryostat increases and so does the temperature.

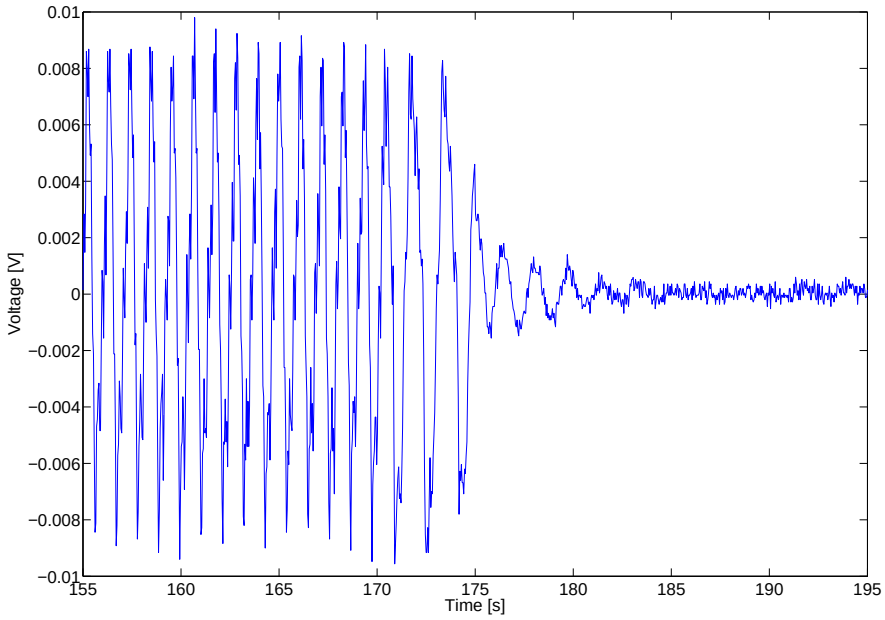

Figure 4.3.: OST signal during the shutdown of the vacuum pump. It takes about 15 seconds for the corresponding 50 Hz noise to vanish.

The velocity of the second sound wave does strongly depend on the predominant temperature in the helium II, especially above about 1.8 K. Its exact behavior has been studied in several experiments in the past. Figure 4.4 gives the result of an experiment described in [17]. One can determine a rather stable plateau for the velocity between 1.5 and 1.8 K which is highlighted with a red frame. This region has been chosen as a compromise for the data taking procedure. For practical reasons, the pressure interval of 5 to 16 mbar was selected. It lies inside the corresponding temperature interval [1.5 K, 1.8 K]. So whenever the vapor pressure inside the cryostat reaches 16 mbar, it is lowered to 5 mbar by restarting the pump. Subsequently, the pump is switched off again and after about a minute the first heat pulses are generated. Both, the pressure decrease from 16 to 5 mbar and the inverted process, the vaporization

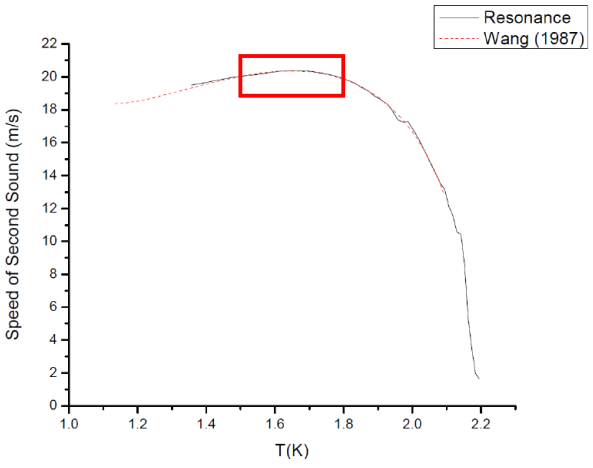

Figure 4.4.: Second sound velocity versus temperature from [17], the used temperature interval is highlighted.

back to 16 mbar, take about 15 minutes. This is an acceptable time window for the experiments. The velocity in the selected temperature frame, determined by the precision measurements of Wang et al. (given in [31]), alters between a maximum of 20.37 m/s and a minimum of 19.83 m/s. The measurements are represented by the dashed line in figure 4.4. The values correspond to a maximum difference of $\Delta v = 0.44\,\mathrm{m/s}$ and a relative deviation of 2.2 % motivating the errors in the later distance measurements.

All the methods combined, so the pump stopped, the power grid disconnected and the circuit shielded, result in a much better signal to noise ratio. An example OST response to a heat pulse including all these hardware enhancements can be found in figure 4.5. Additionally to these solutions, it has proven itself to be very useful to take multiple signals and average them with the recording oscilloscope. This is possible, as the shape of the signals does not change for a fixed distance in one measurement. Another method is to use the so called "high resolution mode" of the deployed TEKTRONIX device. It works basically as an internal averaging over each sampling interval. Both methods and their positive effects are described in more detail in [22]. As they do not affect the intrinsic characteristics of the signal and are of less use for a direct comparison to the results at the Cryolab at CERN, their analysis will be left out at this point.

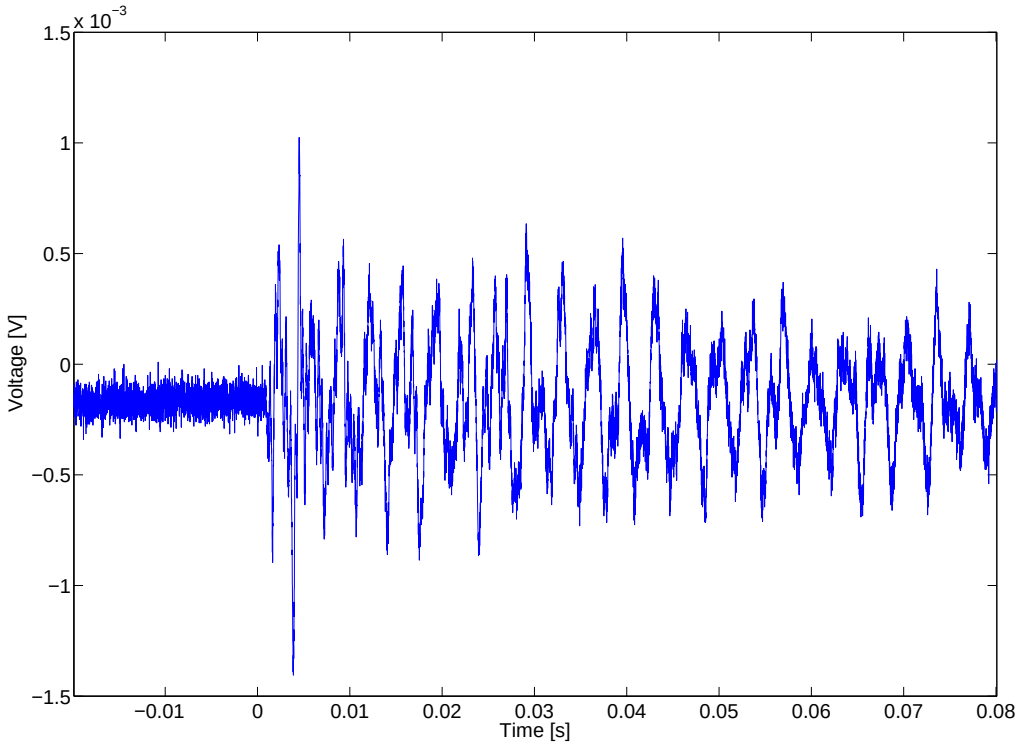

Figure 4.5.: Second sound signal with all setup improvements of February 9^{th}, 2011 at $\approx 1.6\,\mathrm{K}$.

By looking at the maximum amplitude of the noise in the OST signal in the time interval before the heat pulse arived at the OST and comparing it to the first peak-to-peak

value of the actual second sound signal, one can evaluate how good a threshold scan could resolve this signal. For the measurements at Göttingen the final result with the improvements is averaged over distances from 3 to 303 mm between the OST and the SMD heater and over about 16 signals taken at each distance. Its numerical value is:

$$\frac{S_{Amp}}{N_{Amp}} = 2.3 \pm 0.7$$

with S_{Amp} standing for the signal and N_{Amp} the noise value. Only the very first resolvable amplitudes of the second sound wave signal are taken into account for the peak to peak values, as they define how precise the time of flight can be determined.

4.2. Distance Variation

The working principle of a heat source localization via second sound is based upon distance measurements using OSTs. For the determination of any distance, two parameters have to be observed at the same time, the time of flight of the second sound wave and its velocity. The latter can be derived from the temperature in the liquid helium. The second, the time of flight, so the time it takes the wave to travel to the OST sensor after it has been generated, depends on two values again. The first is the moment the entropy wave is created, so some sort of trigger event. In the described experiments it is the heat pulse provided by the function generator. The second and usually harder to determine parameter is the point in time when the first wavefront of normal fluid helium hits the superleak membrane.

In the test setup at Göttingen, measurements of the OST's signal for different distances between the membrane and the heat source were performed. The motivation was to simulate an unknown distance between the OST and a quench spot on a cavity's surface. The temperature is derived from the vapor pressure and kept between 1.5 and 1.8 K as described earlier. To compare the results of the second sound distance computation to the real situation, the distance was measured manually at the setup. During the running experiment only the top part of the OST holding metal rod, that is outside the cryostat, can be measured. A maximum error of 3 mm has been assumed for the analysis. It combines the error of the scale used to measure the steel rod and the different thermal contraction behaviors of the niobium wires and the rod itself [21].

Figure 4.6 shows as an example of twelve signals recorded in high resolution mode [25] on February 9$^{\text{th}}$. The adjusted distance increases from 3 to 183 mm from top to bottom of the presented diagram. The second sound signals themselves last apparently longer than the couple of milliseconds that are shown in the figure. This means that the excited membrane oscillates for a time longer than the recorded one until it returns to its initial position. At the beginning of each signal, a sort of transient effect can be seen. It takes a short moment for the system to reach the maximum amplitudes. Comparing the height of the amplitudes for increasing distances, one finds that they decrease until

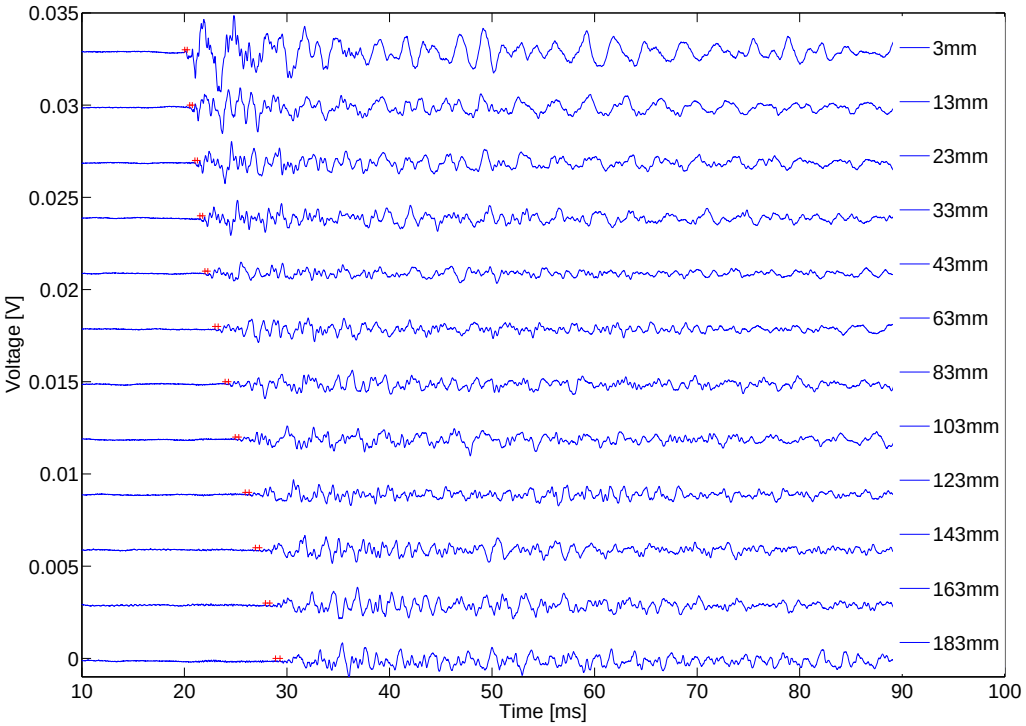

Figure 4.6.: 12 signals of different distances taken at February 9$^{\text{th}}$ in one diagram: The signals are shifted to separate them, the red crosses in each channel mark the time interval in which the signal start is expected including the error in the distance and the velocity interval covered in that measurement. The kink in their vertical connection is due to a change in the step size. The heat pulse was generated at 20 ms.

a distance of about 4 cm. After that distance the changes alter a bit. The amplitude stays stable, respectively decays much slower than before with growing distance. This behavior can be explained with a transition from a spherical to a plane wave character of the second sound wave. In detail this means that as the heat pulse is created in a point like spot — the SMD resistor —, the second sound wavefront propagates on a spherical surface in all directions away from its start. Depending on how close the membrane with an active diameter of 19 mm is to the resistor, it "sees" the wave in a different way. For small distances, small in comparison with the membrane's spatial extent, the spherical wave character will be recognized. The wavefront is going to reach different sections of the membrane at different times and its intensity decays fast for gaining distances. For larger distances the wavefront exciting the flexible membrane can be regarded as a plane one and the intensity losses for the signal become smaller. The development in the relation between the membrane's diameter and the covered upper opening angle of the second sound wave sphere is illustrated in figure 4.7. The curve follows the phenomenon

observed among the signal's amplitudes, as it quickly drops below 10 % within the first 50 mm of distance.

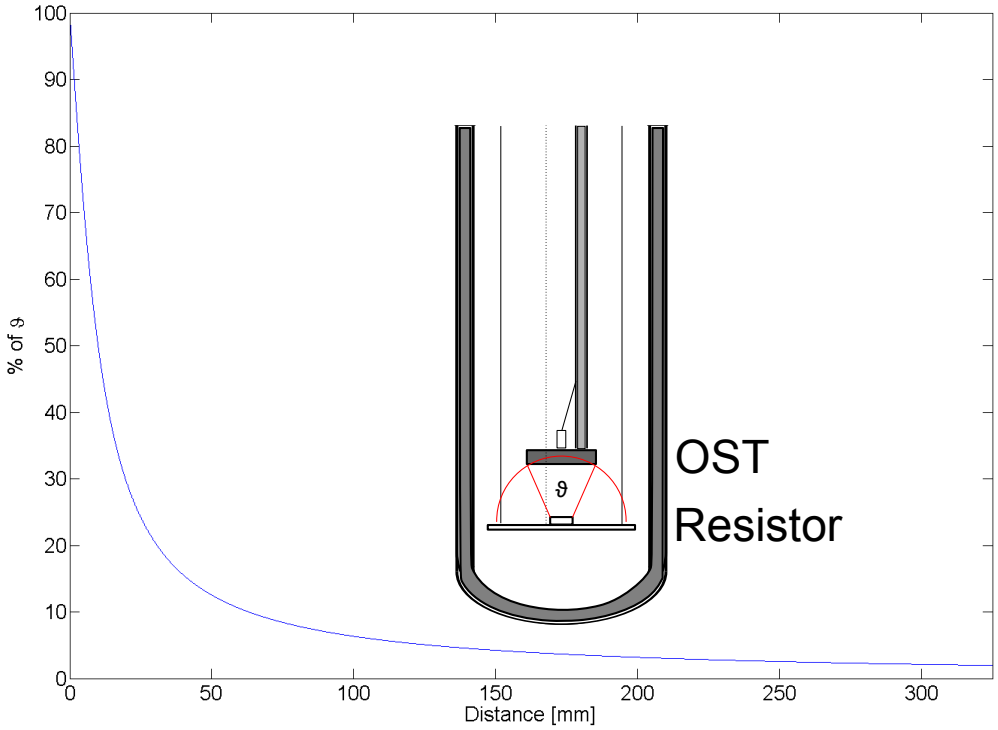

Figure 4.7.: Percentage of the upper polar angle ϑ that is covered by the OST's membrane versus the distance between OST and SMD. The scheme illustrates the situation in the cryostat.

The red crosses in each channel in figure 4.6 represent the expected signal start. This expectation is derived from the set distance including its error and the known velocity for the temperature range including a deviation of it given in [31]. The earliest possible signal start is calculated using the highest possible velocity in the temperature interval and the smallest distance with respect to the error in measurement. The same is done for the lowest possible velocity and biggest distance. The results are marked as "fast" and "slow" signal, compare figure 4.8. This does also explain the increasing size of the highlighted interval for bigger distances. The OST's response at the interval between these points tends to show minor differences from its behavior earlier in time. Nevertheless, the bigger amplitudes — so the resolvable changes — are always delayed. This is the strong hint for a transient effect in the mechanical oscillator.

In order to quantify this deviation, a threshold scan algorithm has been developed. It analyzes the pure background signal prior to the heat pulse trigger and scans for amplitudes larger than five standard deviations around its mean value. The same code has been used for the data taken at the Cryolab at CERN — compare section 5.2.

The results of the threshold scan are compared with the predicted signal starts. The deviation in time from the first and the latest expected signal start is multiplied with the corresponding velocity to express it in terms of a distance. The outcome for both extremes is averaged over two series of measurements and presented in figure 4.8. The total error is a combination of the error in distance and velocity as well as the time resolution of the oscilloscope. The absolute values show an interesting behavior as the slow increase up to about 20 mm until a distance of about 60 mm between OST and resistor is obtained. For higher distances the value first doubles itself and decreases again, a trend similar to the one of the amplitudes.

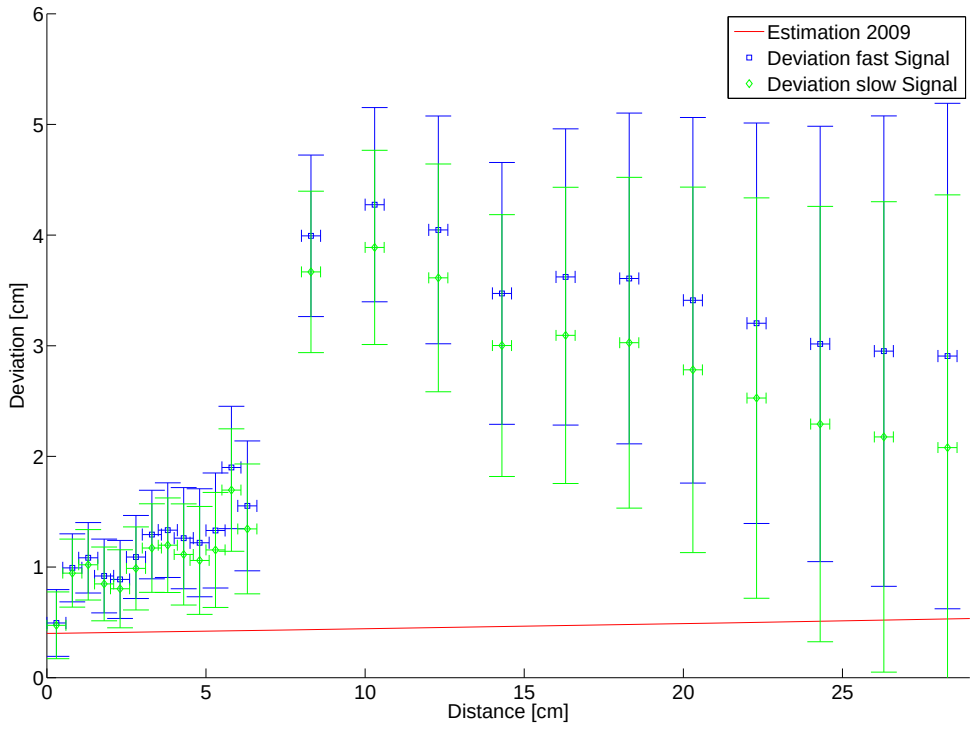

Figure 4.8.: Summary of the distance measurements in the glass cryostat: The deviation between the measured signal and the predicted signal, using the set distance, is shown. For the "fast Signal" discrepancy the highest second sound velocity in the set temperature interval and the smallest distance including the error is used, while for "slow Signal" the smallest velocity and biggest distance is applied. "Estimation 2009" represents the spatial error estimation used for the simulations in [32].

The red line in the plot represents the error estimation σ done for the simulations described in [32]. The estimation is mathematically given by

$$\sigma = 4\,\mathrm{m} \cdot \exp\left(\frac{\mathrm{distance[mm]}}{1000\,\mathrm{mm}}\right). \tag{4.1}$$

It is the error that has been assumed for every individual distance determination in the computer simulation.

The computed deviations are, except for very small distances, much bigger than the prediction from this simulation approach. In fact as they lie in the order of a few centimeters, especially for the interesting distances above 6 cm, they question the precision of the used technique. This may be caused by the very basic readout system, containing no amplification of the signal, and the specific dimensions of the setup.

4.3. Frequency Analysis

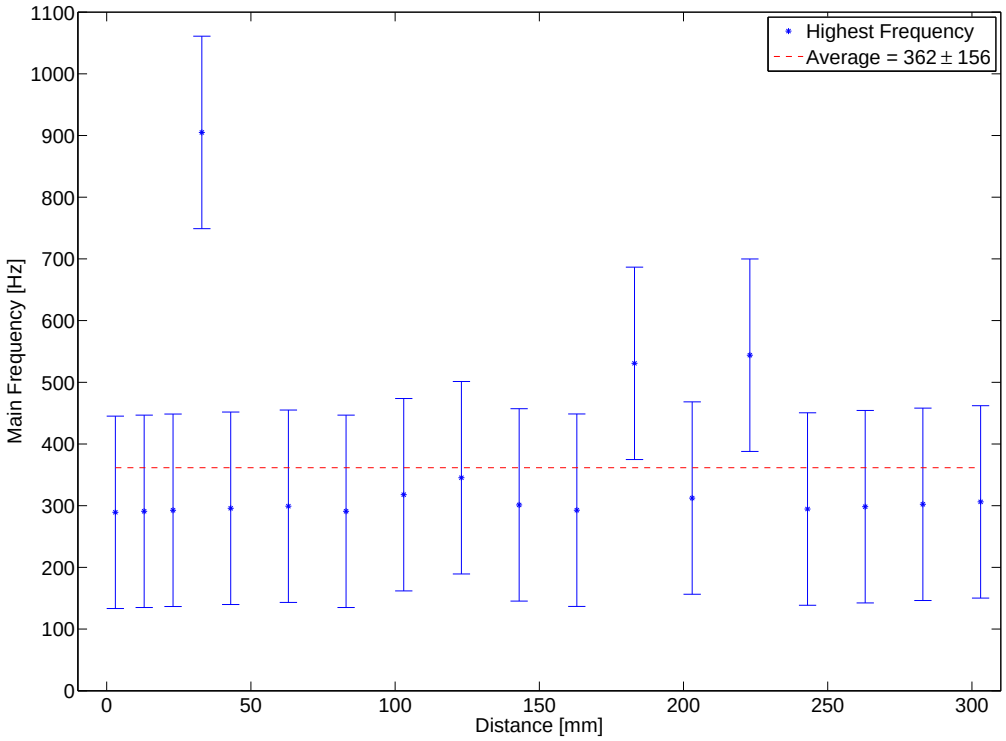

Figure 4.9.: Example of main peak frequency in Fourier space as a function of distance, the corresponding signal was recorded on December 16$^{\text{th}}$, for more details see [22].

For a better understanding of the OST's response to the incoming second sound wave, a frequency analysis of the recorded data for different distances has been performed. Starting with the point in time at which the earliest signal start[1] is expected, the data have been transformed into Fourier space to determine on its dominating frequencies. The complete results for each individual measurement are listed in [22]. Figure 4.9 provides

[1]Compare previous section.

an excerpt of this analysis as it shows the values of the most dominant frequencies versus distance of one series of signals. One observation is that there are three predominant frequencies in the rough order of 300, 550 and 850 Hz — compare the result in figure 4.10. This does not change with increasing distance, at least not in the covered scale. In total, three series of measurements were recorded and analyzed. The final average of their most dominant frequencies is

$$\bar{f} = 372.0 \pm 100.2\,\text{Hz}.$$

This gives a strong hint that the main frequency of the membrane's oscillations is in the order of 300 Hz, a frequency that had to be excluded from earlier analysis as the higher order modes of the 50 Hz noise were also in this regime [21].

Gauss-Window Analysis

For the analysis of the signals recorded at the Cryolab at CERN, a different method was used to perform the Fourier transformation. Instead of taking the complete data after the expected second sound signal start and transforming it, a window of a certain size was moved over the chronological data points excluding the non-covered content. This became necessary since the second sound induced oscillations decayed much faster in the Cryolab measurements than in the experiments at Göttingen — compare figure 5.3. However, this technique can also be used for the Göttingen data.

In addition to the simple window, a weighting procedure using a Gaussian distribution for the Fourier transformation has been developed by Benjamin Willenberg in Göttingen during his work for his Bachelor thesis [33]. In more detail, this method takes the content of each window and applies a weighting with a Gaussian distribution, that has its maximum in the center of the window and a width of the half window size. The size of the windows presented here has been set to $2^{10} = 1024$ data points of the usually 10000 recorded entries per signal. The choice is motivated to gain an acceptable frequency resolution and to accelerate the Fast Fourier Transformation algorithm that favors powers of two [34].

As the window is shifted along the time axis of the signal, each transformation represents a certain interval in the same. To illustrate the signal's evolution in Fourier space and time, these windows can be lined up one after the other as done in figure 4.10. The diagram shows how the frequencies in the $300 - 550 - 850$ Hz domain become dominant at the time the second sound wave reaches the sensor. Additionally, the further behavior of the frequency demonstrates the relatively slow decay of these dominant frequencies. Figure 5.6 shows the same diagram for a signal recorded at CERN. The decay of the membrane's oscillation frequencies is much faster here. Both signals are also illustrated in contour plots of their frequency spectrum in figure 9.3 and 9.4 in the appendix.

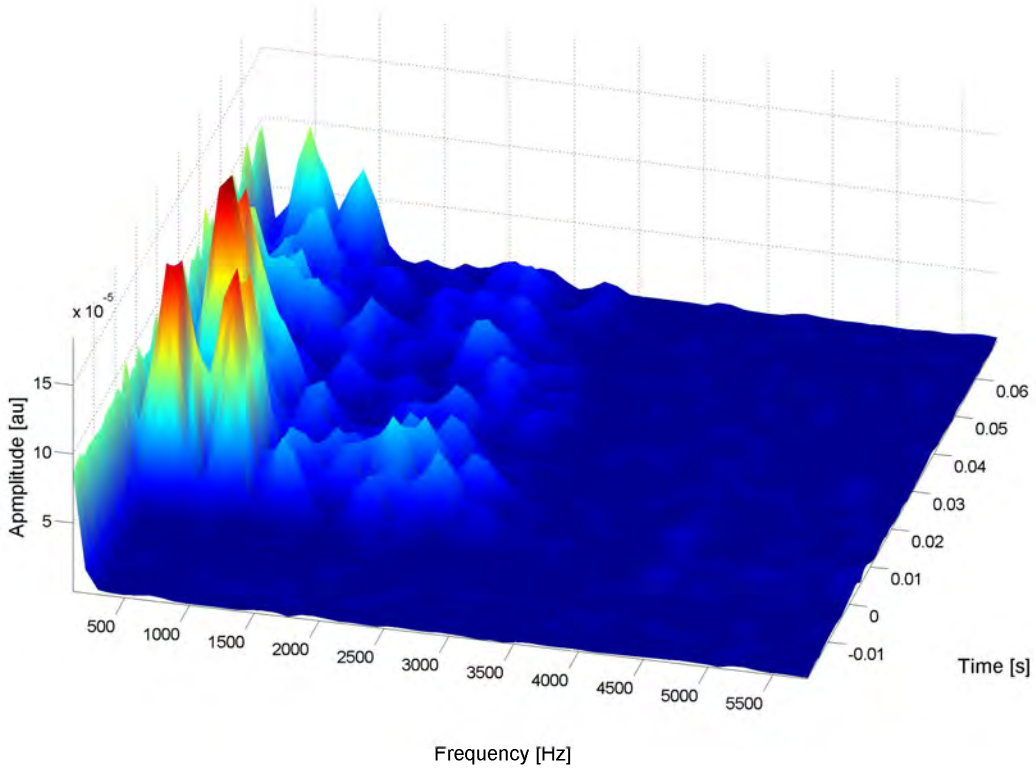

Figure 4.10.: Surface plot for the evolution of the Fourier spectrum per time interval of 1 ms of a typical second sound signal measured in the glass cryostat at Göttingen. See figure 9.3 for a two dimensional map of the same spectrum.

Chapter 5.

Results Cryolab at CERN

5.1. Noise Suppression

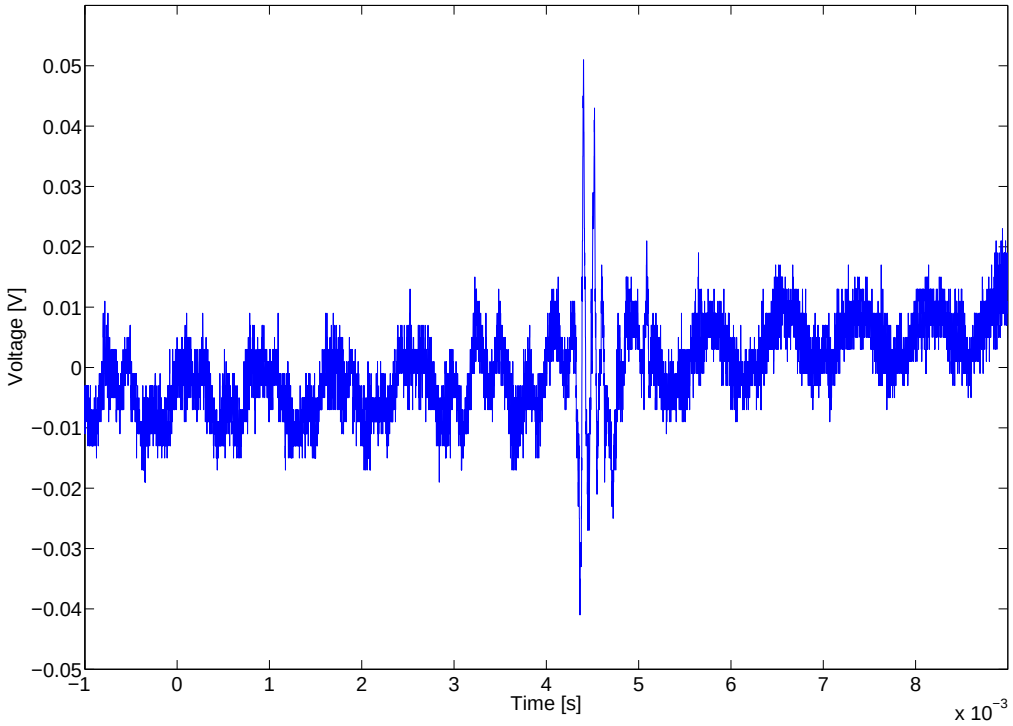

Figure 5.1.: Second sound signal recorded on May 12^{th}, 2011 at $\approx 1.71\,\text{K}$ with the battery for the voltage supply of the OST installed in the amplifier box, but still not separated from the Cryolab ground.

The first results for heat pulses generated with SMD resistors at the Cryolab at CERN had a much lower noise level compared to the signal amplitudes than the early measurements at Göttingen. The gathered experience could be used to optimize the

setup in the first place. Additionally, the used function generator provided a higher output voltage of 10 V and the implemented amplifier increases the OST signal. But although the amplifier helps to separate the actual signal from the common electrical noise, it is also sensitive to any artificially induced disturbance in the OST's response and magnifies them as well.

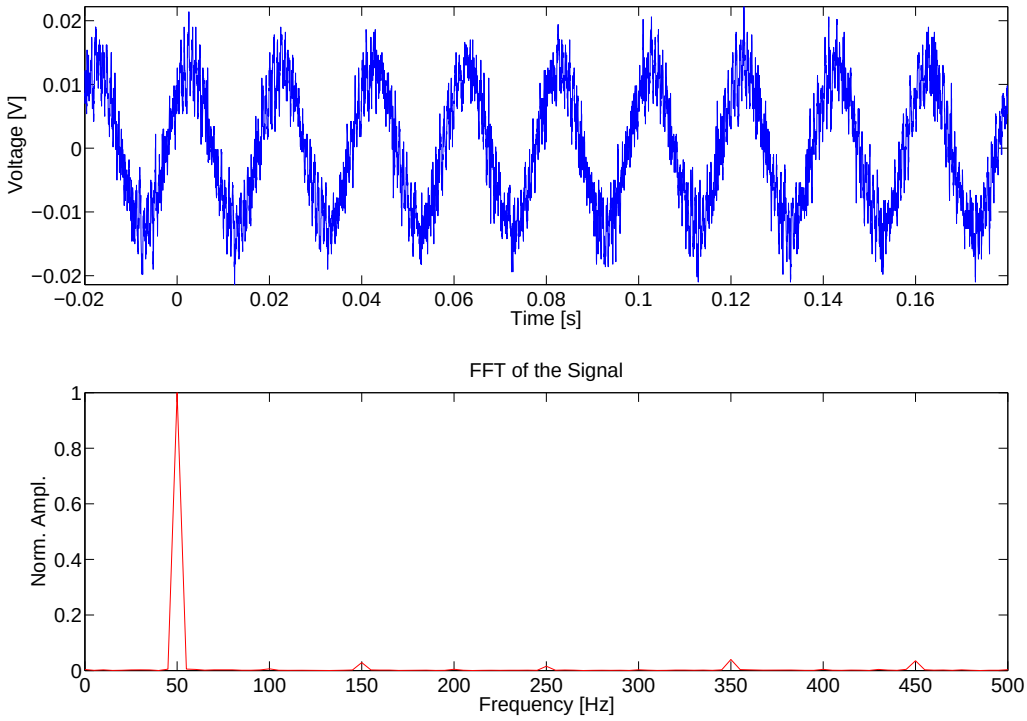

Figure 5.2.: Fourier transformation of the OST noise at room temperature outside the cryostat, connected to the Cryolab ground.

The data shown in figure 5.1 represent the results of these first measurements. The heat pulse trigger is always at 0 s for this kind of representation. A periodical background with a frequency in the order of 1 kHz is evident. In addition to that, the whole signal increases in its absolute value as it lies on the rising slope of another 50 Hz background which is not completely captured in the chosen time frame. Because of this characteristic frequency, the latter one was at first attributed to the vacuum pump as of the results from the Göttingen measurements and since the power supply had already been replaced by a set of batteries. However, the consequently following measurements with the pump turned off, did not show any difference. Obviously, the spatial separation of the pump from the cryostat with a network of several pipes — the system is supposed to serve more than one test stand — is able to absorb any unwanted oscillations. The origin of the periodic noise was found to be the electrical ground connected to the system for safety reasons. Apparently, other devices in the Cryolab interfered with this potential, resulting

in a strong 50 Hz and other higher frequency backgrounds. This could be proven in a special room temperature measurement shown in figure 5.2. Usually the whole insert for the cryostat holding the OSTs was completely insulated after being removed out of the steel vessel. Therefore, it did not show any abnormalities. When the metal frame of the insert was artificially connected to the electrical grounding and the background in the OST's signal appeared.

For any later experiment, the setup was disconnected from the ground by insulating the metal pump line with a plastic junction and two layers of nonconducting material which were put under the metal cryostat. The outcome were much clearer signals as presented in figure 5.3. For a comparison to the results at Göttingen, the ratio of the signal amplitudes at the very beginning of the second sound signal and the maximum noise peaks prior to the heat pulse trigger has been computed. The average value for distances between OST and SMD from 2 to 22 cm is

$$\frac{S_{Amp}}{N_{Amp}} = 10.8 \pm 2.5,$$

an improvement by a factor of approximately four compared to the glass cryostat, as far as the different approaches and setups allow this comparison.

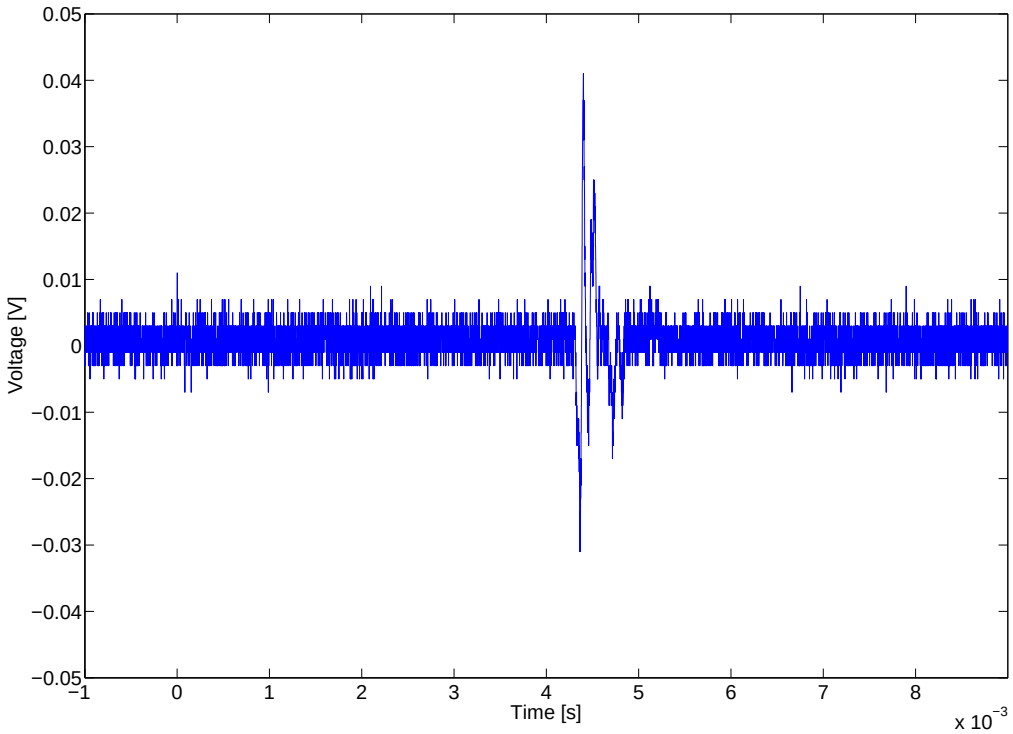

Figure 5.3.: Second sound signal of May 18$^{\text{th}}$, 2011 at ≈ 1.71 K, now disconnected from the Cryolab ground.

5.2. Distance Variation

The first experiments at the Cryolab were done with an OST attached to one of the metal rods of the insert's frame, so at a fixed distance to the heat source. After the major part of the noise had been suppressed, an adjustable metal rod, indicated in figure 3.2, has been added to the setup. With this device, measurements for different distances like at Göttingen could be performed. With the given helium level after lowering the vapor pressure to a few millibar, a variation from 2 to about 22 cm were possible. The set distance was determined at the setup during the preparation phase and during the cool down on the outside part of the rod holding the OST. For the setting, a caliper with a precision of 1/10 mm was used. According to [35], the contraction of the used steel is less than 1 mm per meter for a temperature change from 300 to 4 K. The contraction from 4 down to 1.6 K is even much smaller and can therefore be neglected. As both, the supports holding the copper plate with the SMD boards and the adjustable rod, are completely made out of this steel, a total error of 1 mm has been assumed for the distance.

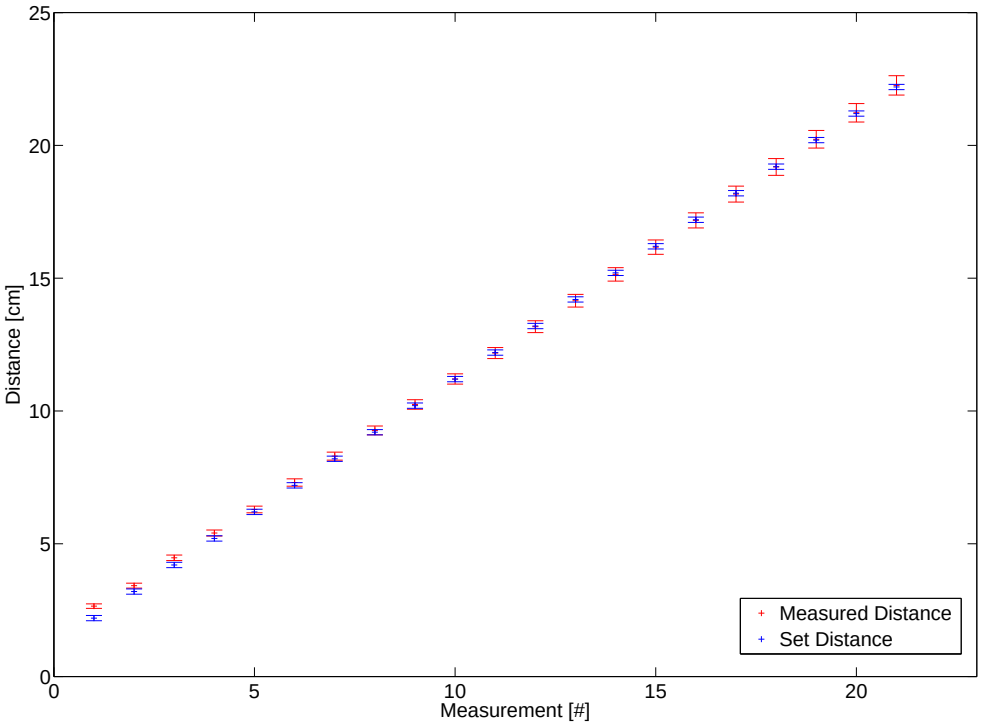

Figure 5.4.: In 21 steps of 1 cm, signals for an increasing distance between heater and OST were recorded. The red crosses represent the results of the amplitude threshold scan, multiplied with the literature value for the second sound velocity, while the blue markers show the corresponding adjusted distances.

The signals recorded for the set distances have been analyzed with the threshold scan algorithm described earlier. The time of flight results were transformed into distance values to compare them with the set parameters. For this purpose, the temperature determined with the installed CERNOX sensor could be used to get a precise corresponding value for the second sound velocity. The error in the velocity and the temperature as well as in the oscilloscope's time resolution were taken into account for the systematical error of the yield presented in figure 5.4. There is no statistical error, as it was not possible to take several measurements for all distances due to the decreasing helium level. Nevertheless, a bigger set of data for a fixed distance of about 10 cm was used to obtain a value for the statistical fluctuation for the threshold scan. The deviation for 20 signals at this constant distance as determined with this amplitude threshold algorithm was less than 14 µs corresponding to an error of less than 0.3 cm. This error has been added to the time resolution error as a rough estimate of the statistical fluctuations.

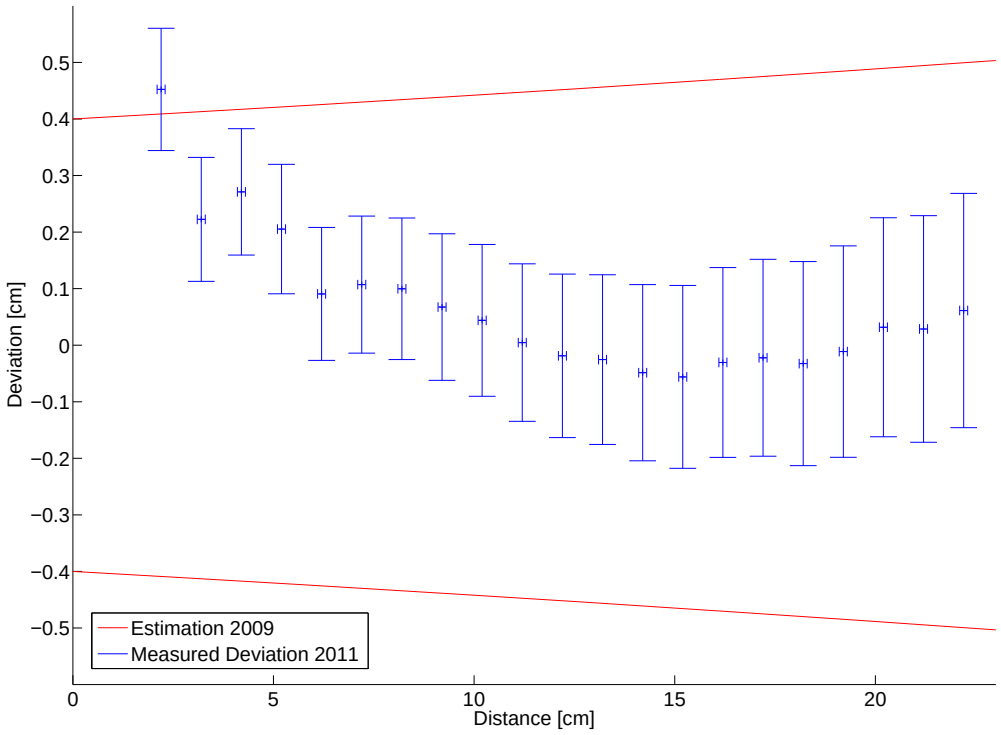

Figure 5.5.: Summary of the distance measurements in the Cryolab: The deviation between the measured signal starts and the predicted signal starts using the set distance is shown."Estimation 2009" represents the spatial error estimation used for the simulations in [32]. As for distances bigger than 3 cm, the values are well below this assumed curve.

Just like for the results at Göttingen, the deviation between the predicted signal start, derived from the set distance and temperature, and threshold scan was determined

for each measurement. As there is no extended temperature and respectively velocity interval to be regarded, no distinction of a "fast" or "slow" signal had to be made. Again, all systematical errors for the set distance, velocity and time resolution contributed to the total error. Figure 5.5 gives the results in comparison to the error of a single distance measurement in the 2009-computer-simulations for quench spot localization [32]. Different from the results in figure 4.6, the determined signal starts are sometimes earlier sometimes slightly later in time than the predicted ones. This and the shape of the signal indicate that there is no omnipresent transient effect or delay for the membrane's oscillations. In the plot in figure 5.5 the values for the deviation are shown. The data shows a similar behavior as the curve in figure 4.7. The latter depicts the percentage of the opening angle above the heater that is spatially covered by the membrane. For small distances, the measured velocity is always less than predicted for a point like sensor. This is also caused by the fact that the relative time difference of the arrival of the second sound wave at the center and at the edge of the membrane is not negligible for these distances. In other words, there is a short delay until the whole membrane, not just its center, has been hit by the first wavefront of normal fluid helium. Especially for distances, which are in the same domain as the membranes own size (diameter 25 mm), this effect becomes visible. Nevertheless, the values themselves indicate a high precision as they are — except for the smallest set distance — all well below 4 mm.

5.3. Frequency Analysis

The frequency analysis of the Cryolab data had to be adapted to the very concise second sound answers. Therefore, the described window scanning of the output signal was used together with the Gaussian weighting from Benjamin Willenberg described in [33]. Since this method focuses on a much shorter time interval than a transformation of the complete recorded frame, the characteristic signal frequencies can be accentuated. This results in a good separation of the signal and background as shown in one example surface plot in figure 5.6. The plot is created by an alignment of the frequency spectra of each window, containing 1024 of the total 10000 data points. The window is shifted step by step by one data point through the complete set, thus the aligned surface plot covers the whole recorded time interval. The frequency resolution is determined by the sampling ratio — in this case 250 kHz — and the window's size (1024). For the given plot the resolution is 244.1 Hz.

The obvious predominant signal frequencies are in the order of 2 and 6 kHz with at least this uncertainty of about 0.25 kHz. To evaluate the dominance of these frequencies, the analysis has been performed with multiple data sets taken at different dates with different OSTs. The main frequencies of the second sound induced signals are given in table 5.1.

Unlike the OST at Göttingen, the OSTs tested in the Cryolab respond to the second sound wave with much higher frequency oscillations. There is large variation between

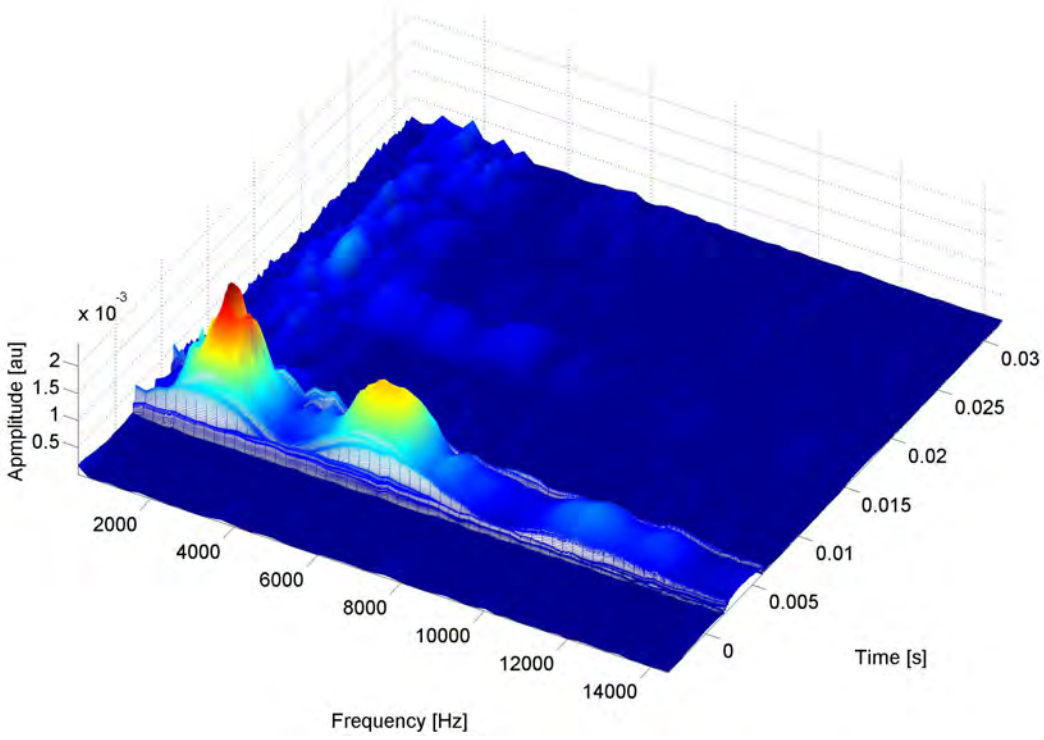

Figure 5.6.: Typical surface plot for the evolution of the Fourier spectrum per time interval of 4 ms of a second sound signal measured in the metal cryostat at the Cryolab at CERN. See figure 9.4 for a two dimensional map of the same spectrum.

Date	Main Frequency [Hz]	# of Samples	Additional Comments
May 18$^{\text{th}}$	9068 ± 2010	7	fixed OST, different temperatures
May 26$^{\text{th}}$	1953 ± 94	26	changing distances
July 26$^{\text{th}}$	1953 ± 281	3	fixed, same OST as in May 26$^{\text{th}}$
July 26$^{\text{th}}$	1221 ± 345	21	changing distances, CERN built

Table 5.1.: Main signal frequencies for different OST measurements.

the individual devices, but all the main frequencies are in the kHz regime. The used amplifier does not change the frequency information of the signal in this range. It cuts out very low frequencies in the order of a few Hertz and cannot conserve high frequencies in the MHz regime. Therefore, no distortion by this device has been observed.

Apparently, the combinations of membranes, casings and electrodes used at CERN bear different characteristics than the OST used in the setup at Göttingen. The Cryolab results point out the individual behavior of the identically constructed devices. However,

the OST, that has been used in two separate experiments, shows a continuity in its second sound response frequency although its placement was changed completely. In the measurements of May 26$^{\text{th}}$ it was attached to the adjustable metal rod while on July 26$^{\text{th}}$ it was fixed to a steel support of the copper plates. This suggests that once assembled, an OST keeps its characteristics for the second sound measurements. Yet, there is not enough data on other OSTs to verify this particular statement.

The CERN OST — the other OSTs did all contain all membranes prepared at CERN while the rest of their structure has been manufactured at Cornell University — features a slightly different main frequency than the others. Albeit the value is still in the kHz range and higher frequencies in the order of 6 kHz can be observed in the signal spectrum as well.

5.3.1. Frequency Threshold

The representation of the evolution of the frequency spectrum in figure 5.6 shows a distinct start of the membrane's oscillations induced by second sound. The dominant response frequency arises very fast in the spectrum. As it marks the arrival of the first second sound wavefront, it immediately suggests itself to use it for a threshold scan similar to the one triggering on the signal's amplitude. A corresponding algorithm for such a threshold scan in the Fourier space has been created. It uses the information gained with the Gaussian-window scan of the signal. For each window position, the strongest frequency is determined. The program searches for values matching a predefined signal frequency, including a small tolerance interval. As this threshold frequency might accidentally appear in the just-noise part of the signal, the algorithm tries to find the first cluster of frequency matching windows that has a certain minimum size. If found, the very first window of this cluster defines the detected signal start. Due to the Gaussian weighting, its center gives the point in time which marks the moment the threshold is reached.

One example of a recorded signal with all three signal starts — the one predicted using the set distance value, the one determined with the amplitude threshold scan and the one identified by the frequency threshold scan — is given in figure 5.7. The threshold frequency has to be determined manually. The results of the frequency analysis, see table 5.1, show that the characteristic frequencies lie in the regime of 1 to 10 kHz. Especially the repeated measurement of one OST suggests, that the individual devices might keep their very own resonance frequency if not dissembled between the measurements. Therefore, the threshold value could be determined in a calibration prior to a real measurement. This would make it possible to apply an automated frequency threshold scan to determine the time of flight of the second sound wave.

Like the amplitude threshold scan, the frequency threshold algorithm has been used to analyze the data set recorded for different distances between OST and SMD resistor. Again, the computed results for the time of flight were compared to the prediction. The deviation has been transformed into a distance value using the velocity linked to the

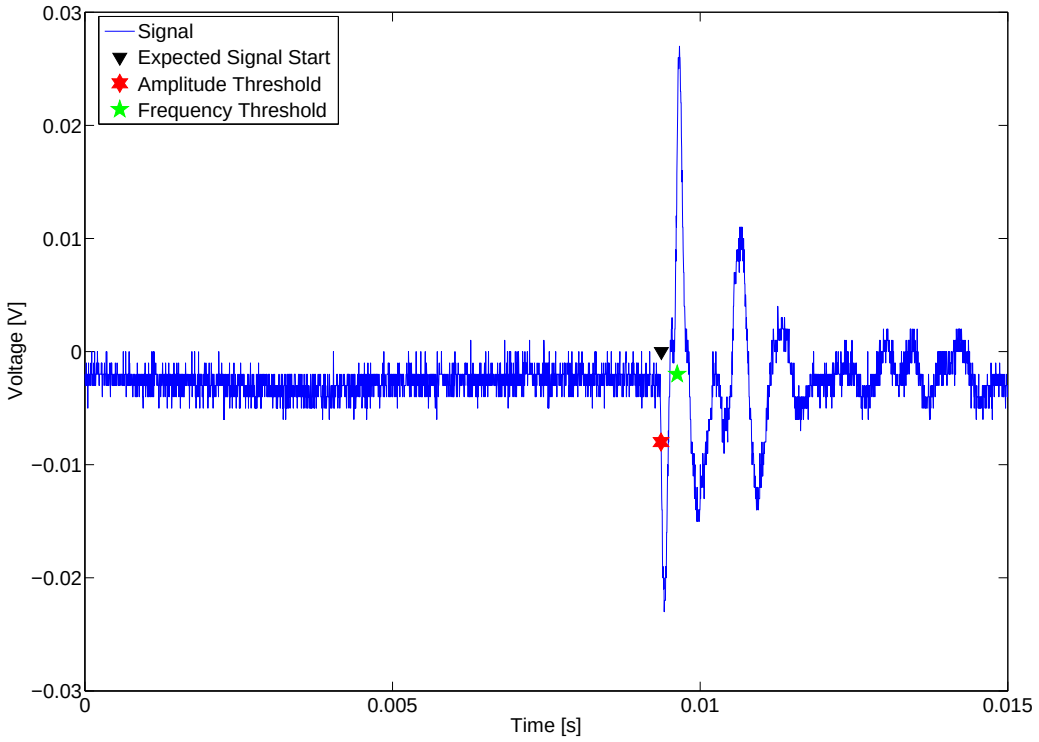

Figure 5.7.: OST response to a SMD heater at a distance of 19.2 cm. The signal has been recorded on July 26$^{\text{th}}$ at a temperature of about 1.67 K. The black triangle indicates the start of the signal according to the literature value of the second sound velocity while the green and the red star represent the result of the frequency and amplitude threshold scan algorithm.

recorded temperature. The corresponding values are depicted in figure 5.8. The red curve is the same as in figure 4.8 and figure 5.5, representing the error estimation of 2009. Similar to the signal starts evaluated with the amplitude threshold scan, the marks set by the frequency scan are not all prior to or after the predicted ones, but most of them are later in time. This can be explained by the need of at least half a wave length of an oscillation to deduce its frequency. The numerical results themselves are not as good as for the amplitude threshold scan. Yet, as the stay under a value of 6 mm for all distances, they are useful too. Additionally, they are actually smaller than the ones originating from the amplitude change in a few cases. A combination of both methods seems reasonable. The frequency scan can be of advantage in case of low amplitude to noise ratio, so for relatively high temperatures as shown in the next section or in a noisy environment.

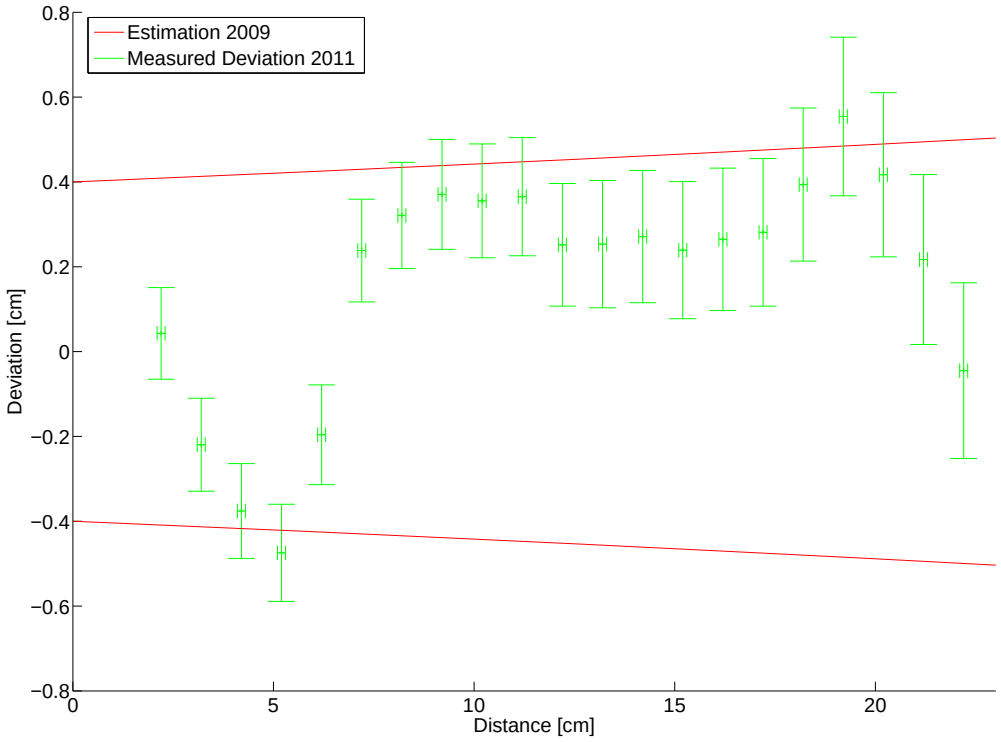

Figure 5.8.: The deviation between the beginning of the signal determined with the frequency threshold scan algorithm and the prediction of the same is shown. "Estimation 2009" represents the spatial error estimation used for the simulations in [32].

5.4. Velocity Determination

In the results of the measurements with a variation of the distance between OST and heater — presented earlier —, the procedure was to determine a time of flight and to use the second sound velocity for the recorded helium temperature to compute a distance value [31]. Another way is to compute the second sound velocity using the set distance value. This serves as another crosscheck if the time of flight agrees with the expectations for it. Besides changing the form of analyzing the results, it is also interesting to use this method to investigate on the temperature dependence of this velocity.

As the resulting amplitude decreases for higher temperatures in helium II — this is caused by the superfluid–normal fluid helium ratio, compare figure 5.9 —, it gets more complicated to resolve the signal from the noise background. A good isolation from any possible noise source is mandatory. Furthermore, the frequency threshold algorithm can be used to separate the actual signal from its background.

Figure 5.10 shows an OST signal recorded at 2.05 K in its upper part. The actual signal starts between the five and the six millisecond mark on the x-axis. The signal's

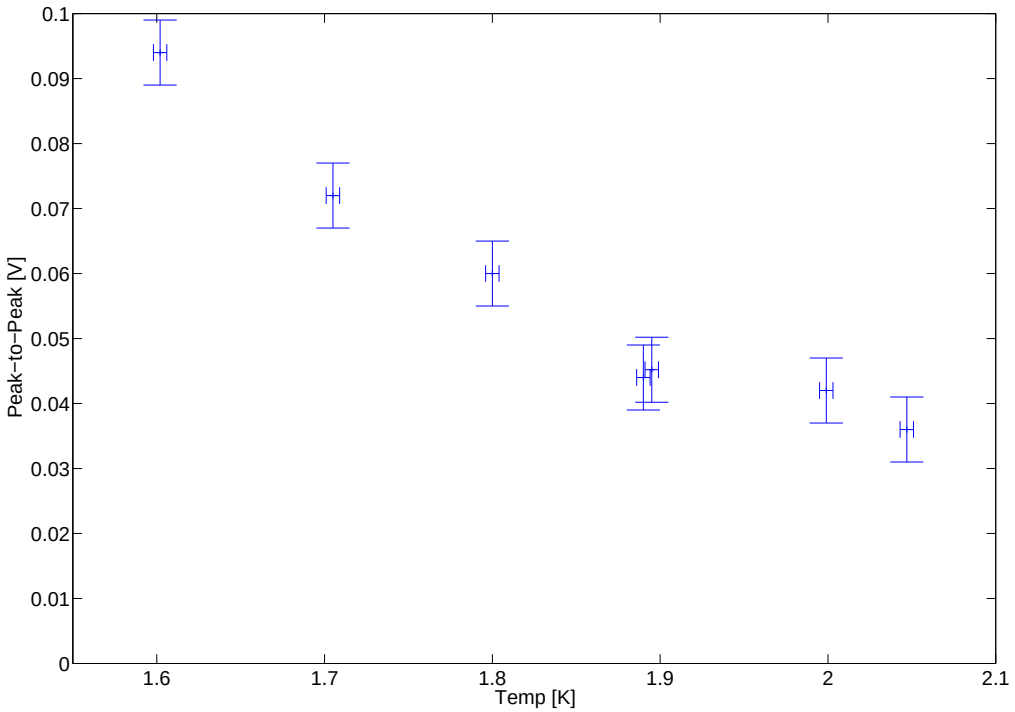

Figure 5.9.: The peak to peak amplitude values of second sound signals for different temperatures. The amplitude increases for lower temperatures as the share of the superfluid helium increases in the mixture, compare [36]

amplitude is barely significant compared to the noise background earlier in the same plot. Looking at the surface plot of the frequency spectrum, which can be found in the lower part of the same figure, a much better distinction can be done. The noise background presents itself as two "walls" in the range of 110 and 220 kHz, ubiquitous in time. At the same time the small changes in the voltage of the OST response — so in the upper plot — arise, three significant peaks appear in the Fourier space. They are in the order of 2, 6.8 and 21 kHz. The frequency threshold algorithm can trigger on one of these frequencies and in this way determine the correct time of flight.

Both, the amplitude and the frequency algorithm, have been applied to data gathered in an experiment recording second sound signals for different temperatures. Their findings have been used to compute the velocities of the second sound wave. The OST, used in the experiment, was fixed at a distance of 8.6 cm from the SMD heater. The results are given in figure 5.11. Except for the highest temperature, the results are in good agreement with the prediction deduced from [31] (including the given error). The average deviation is 0.66 mm/s for the frequency threshold and 0.65 mm/s for the amplitude threshold. With the very low background achieved at the setup, both approaches yield similar outcomes. Nevertheless, for a higher noise rate, this might change.

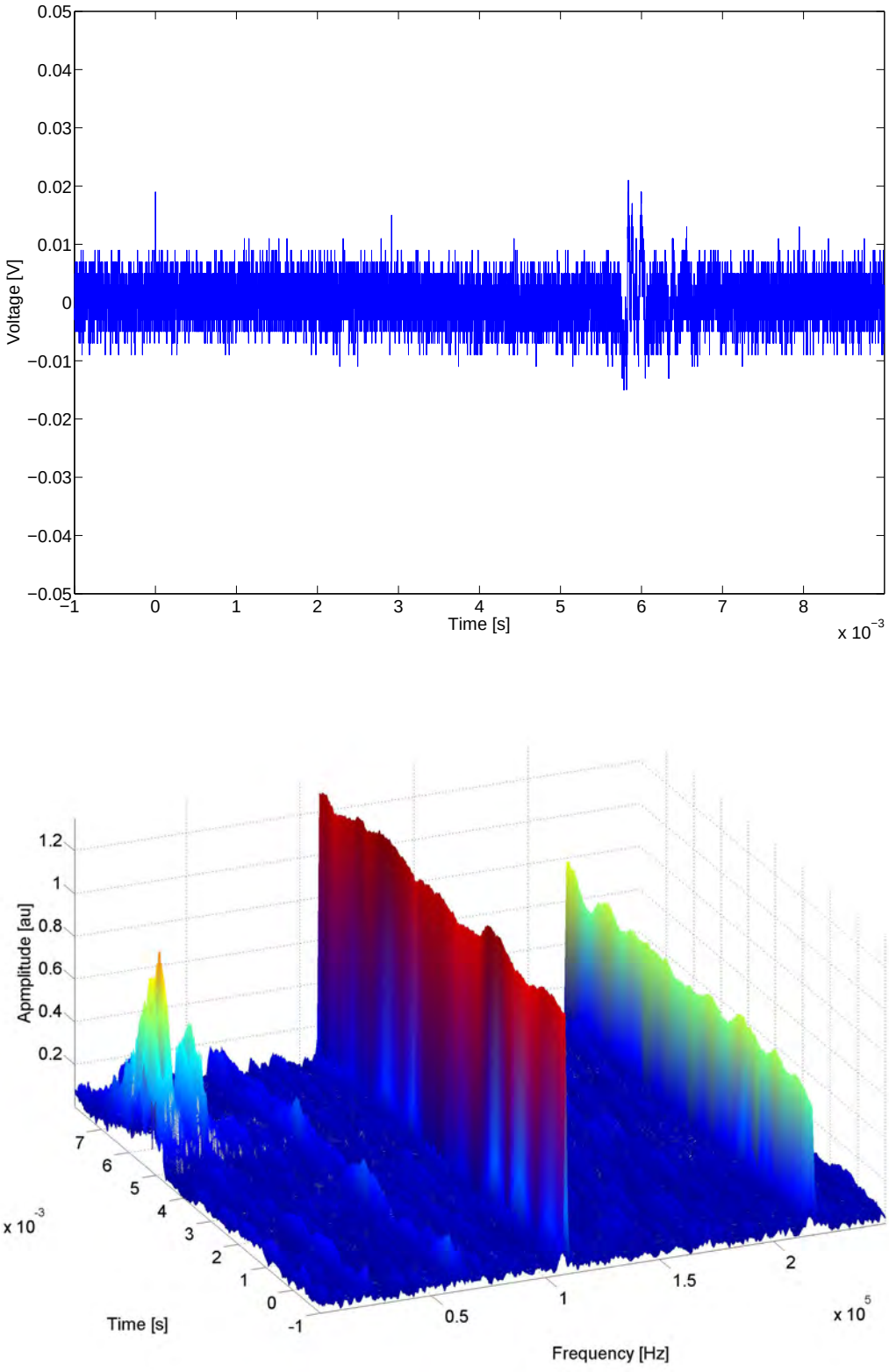

Figure 5.10.: Signal and surface plot of the frequency analysis of the OST response to a heat pulse at 2.05 K: The separation of signal and noise gets much easier in Fourier space.

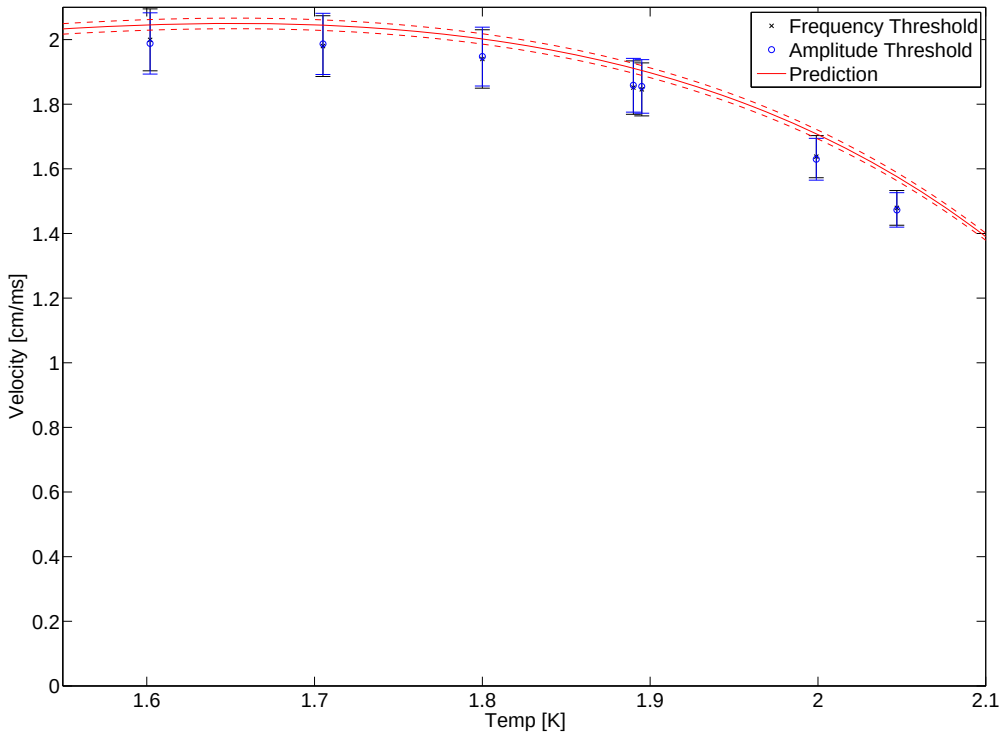

Figure 5.11.: A comparison of the results of the frequency threshold and amplitude threshold algorithms which have been used to determine the second sound velocity for different temperatures at a distance of 8.6 cm on May 18$^{\text{th}}$. Especially for a small amplitude-noise ratio, which occurs at "high" temperatures ($\sim 2\,\text{K}$), the frequency scan yields an advantage over the amplitude scan, compare figure 5.10.

5.5. Electrode: Surface Modifications

Besides the examinations of the amplitude and frequency of the responses of the basic OST to the second sound wave, the influence of modifications of the sensor itself has been investigated. In a study, separate to the other experiments, different conditions of the brass electrode, so the fixed plate of the OST "capacitor", have been tested. The idea was to determine how the actual texture of this electrode affects the height of the measured amplitudes. As the sputtered membrane touches the electrode directly as soon as the voltage of 120 V is applied, its attributes influence the oscillations excited by the second sound and determine the device's sensitivity.

Two different approaches were tested in the experiments. The first was to create a well defined roughness on the electrode's surface. This has been realized with a perforated

Kapton[1] foil which is inserted between electrode and membrane, see figure 5.12. The foil has holes with a diameter of 0.1 µm and a distance of 0.2 µm between each of them in every row and column, forming an evenly distributed grid. The assumption was that these small pits might emphasize the membrane's oscillations as they provide more space for the superfluid helium II. The result however, given in table 5.3, proved the contrary.

The second approach was to reduce the average distance between the gold layer i.e. the flexible plate and the electrode by polishing the latter. After the OST manufacturing, the electrode has still some circular structures remaining on its surface from the machining process. These irregularities change the local distance between the plates and because of that the total capacity of the OST. As mentioned in the theory part (equation 2.1), the charge on the OST plates is constant for short time periods:

$$Q = C \cdot U = \text{const.}$$

This leads to

$$\Rightarrow \qquad \frac{\mathrm{d}U}{U} = -\frac{\mathrm{d}C}{C},$$

while

$$\mathrm{d}C \sim \frac{\mathrm{d}d}{d^2}.$$

This means that changes in the capacity correspond to inverted changes in the recorded voltage. These changes are then proportional to one over the squared distance d between gold layer and electrode. In order to have a significant change in the signal, so at least a factor of two for the amplitude,

$$2\,\mathrm{d}C_b = \mathrm{d}C_a$$

has to be fulfilled, with b marking the state "before" polishing and a the one "after". Assuming

$$\mathrm{d}d_b \approx \mathrm{d}d_a,$$

results in

$$\Rightarrow \qquad \sqrt{2}\,d_a = d_b.$$

d_b and d_a can be written as

$$d_b = d_m + x, \qquad d_a = d_m + y,$$

where d_m is the thickness of the membrane and x and y represent additional space due to the irregularities on the electrodes surface. According to Whatman, the used membrane

[1]Kapton is a registered trademark of E. I. du Pont de Nemours and Company.

type has a thickness of 6 to 11 µm. For simplicity reasons 10 µm can be assumed:

$$d_m \approx 10\,\mu\text{m}$$

Isolating x, the pre-polishing parameter, gives

$$\Rightarrow \qquad x \approx 4.1\,\mu\text{m} + \sqrt{2}\,\text{y}.$$

The used polishing method is supposed to level the surface with a deviation of less than 0.1 µm, compare figure 5.13 and table 5.2.

$$y \approx 0.1\,\mu\text{m}$$
$$\Rightarrow \qquad x \approx 4.3\,\mu\text{m}$$

So in order to double the amplitude, the distance to the gold layer has to be reduced by at least 4.3 µm, given that the according flatness can be achieved with the treatment.

Figure 5.12 shows photographs of the four different electrode variations that were tested at CERN. The left most electrode represents the standard situation with no special treatment. This electrode has been used in an OST for a reference measurement. The second electrode shown, has been polished. The third has been polished as well, but covered with the described Kapton foil. The fourth picture shows the first electrode again, but after a polishing procedure.

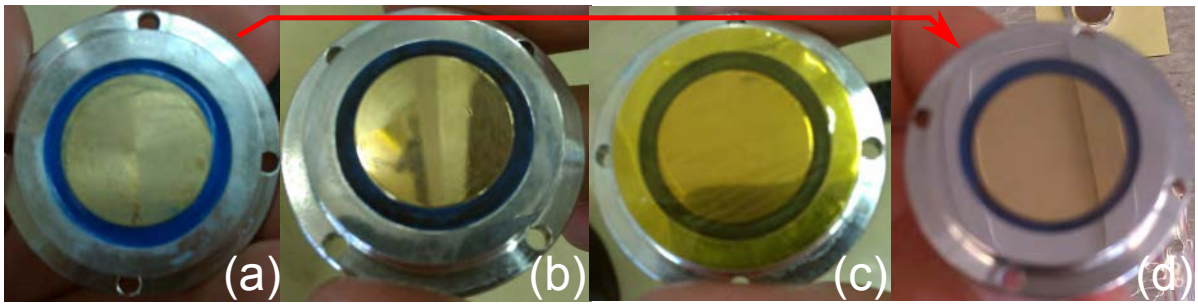

Figure 5.12.: Pictures of (a) the normal electrode, (b) the polished electrode, (c) the electrode with the Kapton foil — with a polished electrode underneath — and (d) the normal electrode again, after treatment, compare [37].

To check if the target roughness of 0.1 µm had been achieved by polishing, a normal electrode and the polished one were examined with a white light scanning profilometer. The device — a Veeco Wyko NT 3300 — has a vertical resolution of up to 0.1 nm [38]. Figure 5.13 and table 5.2 summarize the results of the representative scan. The average roughness of the non-polished electrode is in the order of 1.3 µm but the maximum deviation given in table 5.2 and figure 5.13 show that single circular shaped elevations can increase the distance much more. The surface of the polished electrode has even smaller irregularities than assumed. The requirements for a significant increase of the signal's amplitude by a factor two or more can be met.

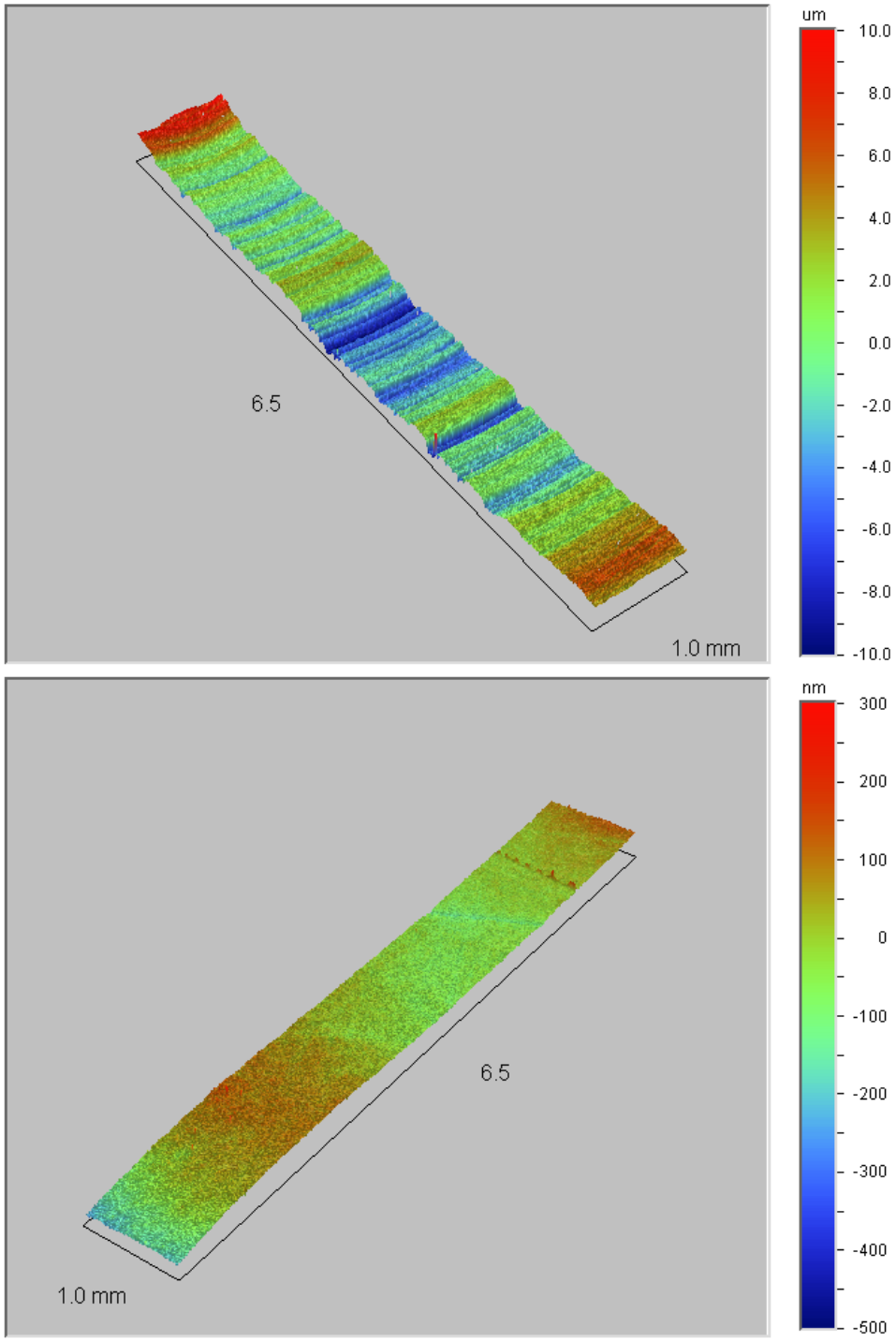

Figure 5.13.: Screen shots of the profile measurement of a normal OST electrode (upper part) — the circular shape of the irregularities can be identified — and a polished electrode (lower part).

The size of the cryostat used at the Cryolab allowed to install three OSTs and three pairs of heaters[1] at the same time. Two measurements were performed, one with the

[1]The two different SMD resistors are described in part I.

Electrode	Average Roughness	Maximum Deviation
Normal Electrode	$1.3 \pm 0.1\,\mu m$	$11.1 \pm 4.4\,\mu m$
Polished Electrode	$10.5 \pm 1.3\,nm$	$98.3 \pm 26.6\,nm$

Table 5.2.: Results of the profile measurement of two different OST electrodes.

first three versions of electrodes in figure 5.12 ((a) to (c): June 17th) and one with the last three ((b) to (d): July 7th). The purpose of the second experiment was to verify the results of the first. Therefore, the reference electrode has been polished in between and the Kapton foil has been moved from the first ((c) in figure 5.12) to the second electrode polished at DESY ((b) in the same figure). In each measurement, each OST has been excited by an SMD heater at a distance of 122 mm for different temperatures of the helium. For a comparison of the results, the maximum peak to peak values of the signals of the different electrode featuring OSTs were normalized with the ones from the reference OST (a). Their ratios are given in table 5.3. The values are averaged over the two sessions and the used temperature interval between 1.6 and 1.8 K.

Heater	Normal Polished	Kapton	Polished
R1: 1/8 W	3.5 ± 0.2	0.8 ± 0.1	2.1 ± 0.2
R2: 1/10 W	2.7 ± 0.1	1.2 ± 0.1	3.1 ± 0.3

Table 5.3.: Peak to Peak ratios of the signals for different electrode constellations, "Normal Polished" represents the reference electrode which has been polished for the second measurement, "Polished" represents the average achieved with the electrodes polished at DESY, compare figure 5.14. All ratios are with respect to the reference device.

While the Kapton foil, so the evenly distributed roughness on the electrode, has not resulted in any improvement, the polishing procedure produced a mean gain by a factor of 2.9 ± 0.1. This is even more than expected. A direct comparison of the maximum amplitude difference for the reference OST before and after polishing is given in figure 5.14. The results favor a polishing of the electrodes of all OSTs in further experiments. More details can be found in [37].

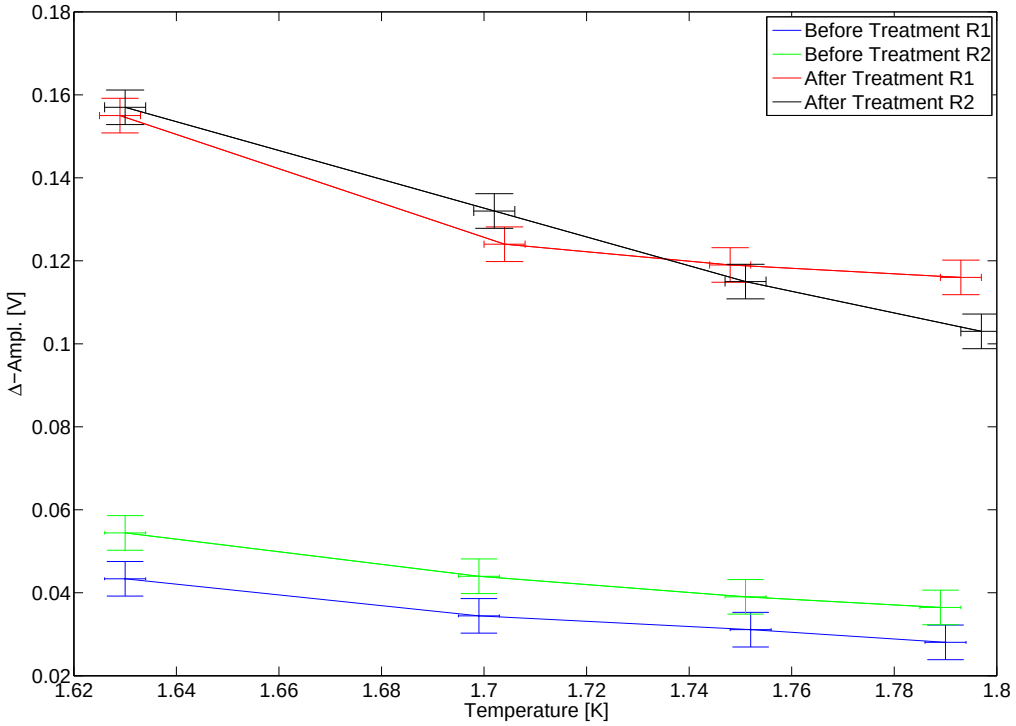

Figure 5.14.: A direct comparison of the peak to peak measurements of the OST with the normal electrode before (June 17^{th}) and after polishing (July 7^{th}) for the two used SMD heaters, compare [37].

Chapter 6.

Setup SPL-Cavity at CERN SM18

6.1. OST Manufacturing

The final step for the heat source localization with second sound is to take a real cavity and try to find quench spots on its surface with the help of OSTs. At CERN, the current project is to perform second sound measurements with an SPL prototype cavity. The cavity itself is a pure niobium single-cell structure. Its resonance frequency is 700 MHz, so in the same order as for the SPL five-cell design. The actual dimensions are different from the SPL cells since it is a research and development prototype, which mainly serves the purpose to investigate on a bulk niobium cavity in the particular frequency range. It has been developed and built at the Saclay CEA research center in France and is lent to CERN. The cryostat for the cavity test is placed at the experimental hall SM18 .

The cavity has been fixed in a metal frame — see figure 6.2 — and evacuated for a measurement in a vertical test stand. For a simultaneous second sound measurement, a number of additional OSTs had to be manufactured at CERN as the existing ones were not sufficient in quantity and some of them already in use at the Cryolab. The only change that was made to the initial design of Cornell University during this process was to replace the SMA plug by a Lemo series 00 plug like it has been done before at Göttingen [22]. In total twelve brass electrodes, casings, consisting of the aluminum back and ring and sixteen membranes were prepared. The devices were assembled in the following order:

1. The Lemo plugs are soldered to the electrodes.
2. These are glued into the back of the aluminum casing with a Stycast 2651MM general purpose epoxy encapsulant.
3. Finally, the membranes are attached to the sensor with the aluminum front ring and four stainless steel screws.

Figures 9.7 to 9.10 in the appendix illustrate the assembling process. As this was done before the investigations on the electrode enhancements were accomplished, none of the installed electrodes were polished beforehand. Nevertheless, it was of great importance to gain the experience how to manufacture the complete OSTs from scratch. Additionally

to the described steps above, eight of the devices were equipped with special steel sleeves, as shown in figure 9.11, to attach them to the metal frame of the single-cell cavity.

Before installation, all newly manufactured OSTs were tested with the amplifier box at room temperature. After that, eight of them were mounted on the metal frame of the cavity around its equatorial region as shown in figure 6.2.

6.2. Considerations for the OST Installation

Like presented in section 5.4 the velocity of the measured second sound wave can be determined not only in dependence of the temperature but also of the set distance between the heater and the membrane. The results of such a measurement are presented in figure 5.11.

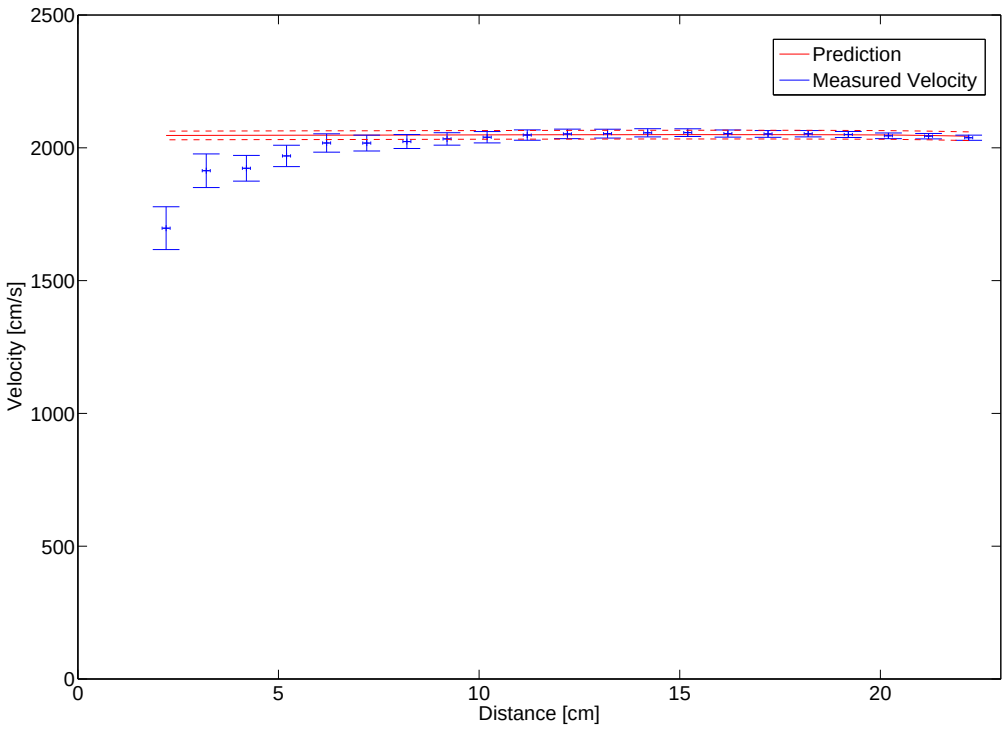

Figure 6.1.: Results of a direct velocity measurement as a function of increasing distance: Since the absolute error in the determination of the time of flight entails a big relative error in the velocity, the systematical error increases for smaller distances.

The results of the amplitude threshold scan are very similar — although inverted — to the trend in the coverage of the opening angle above the SMD heater shown in figure 4.7. For distance in the regime of few centimeters, the OST cannot be regarded as a

point like sensor anymore as its spatial expansion is in the same order. For the setup with the cavity this implies, that the smallest distances from the OSTs to the surface should be chosen big enough to avoid this effect. The further results for larger distances show that they do not cause any limitations. Therefore it is consequently of advantage to leave a certain distance between cavity and sensor, as the area of the surface that is directly seen by each OST increases this way (compare proposed geometry in [32]). For the presented setup, which is supposed to be a first test of the whole method, the geometry of the metal frame determined the chosen distance. The resulting minimal gap between the membranes and the niobium is not smaller than 4.5 cm, an acceptable situation as to the results presented above.

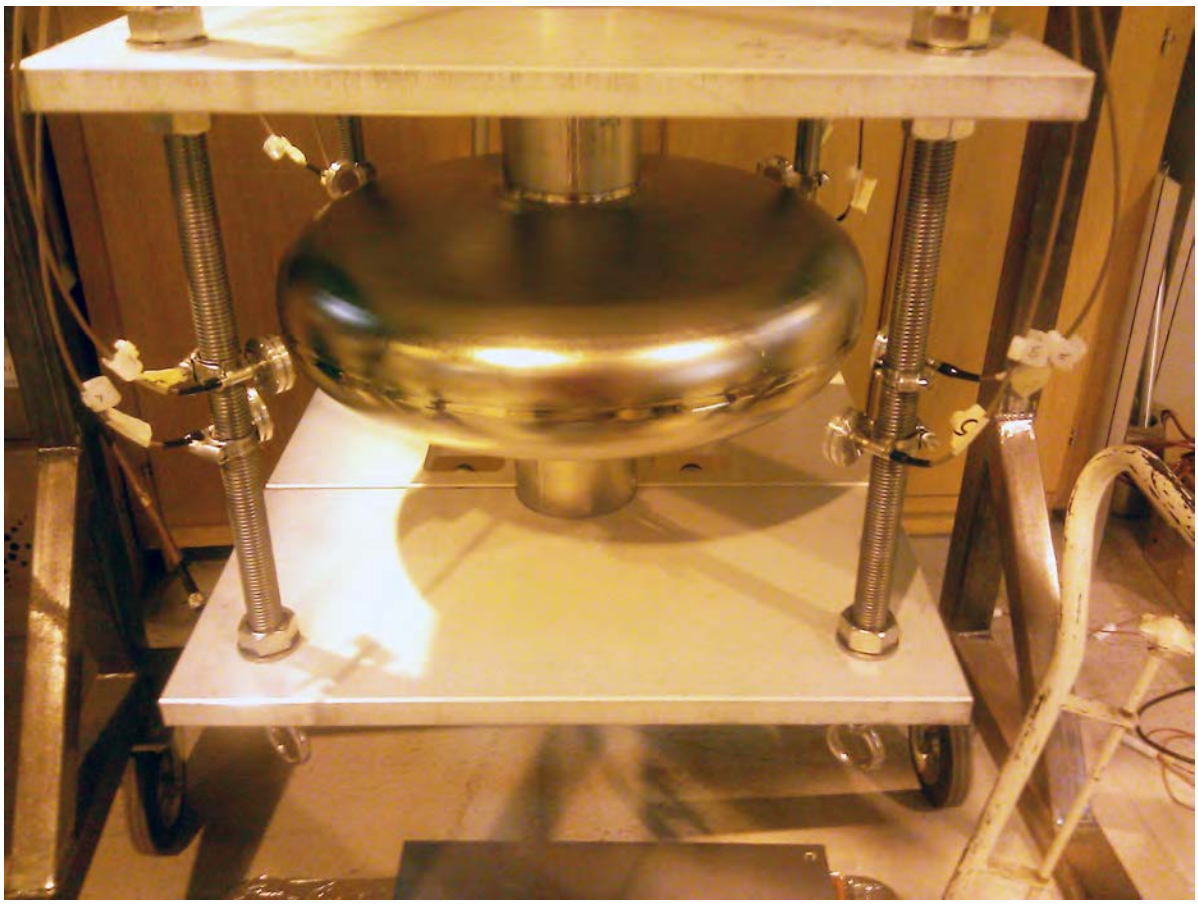

Figure 6.2.: Picture of the SPL single-cell setup with eight installed OSTs at SM18.

The cavity is mounted on a large insert including all necessary vacuum and rf connections to operate it. The OSTs are all connected to one socket on the top cover of this insert. This socket is directly connected to the amplifier box, which contains the batteries for the voltage supply of all second sound detectors. The eight channels of the box are finally read out by a PXI (PCI eXtension for Instrumentation) from National Instruments at the setup. At the PXI, either the reflected power or transmitted power signal of the cavity can be combined with the OST signals to trigger the measurement in

case of a quench. The whole system can be controlled remotely from the control room at SM18. The software solution for the data acquisition has been developed in LabVIEW by Karol Krizka during his summer student program in 2010. As it exports the recorded data in plain text form, the further processing can be performed with any other software as well. In order to combine the data with the other algorithms described in this thesis, a three dimensional representation of the cavity's setup has been created in MATLAB, see figure 6.3. It uses the exact geometrical parameters of the installed cavity. A similar model has been created for the SPL five-cell cavity, see figure 9.14 in the appendix. This representation can be combined with triangulation algorithms also developed in MATLAB at DESY, Cornell University or Göttingen. But prior to the analysis, the test stand has to be put in operation. This includes a temperature monitoring of the helium which has to be combined with the second sound measurements in order to obtain a value for the propagation velocity.

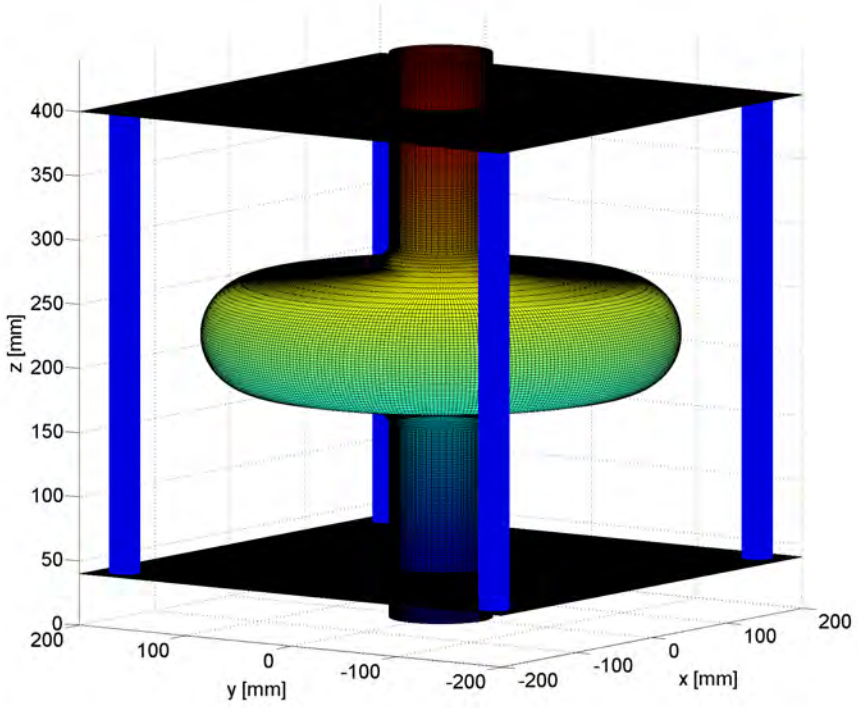

Figure 6.3.: Matlab figure of the SPL single-cell surface at the according installation.

Part III.

Conclusion

Chapter 7.

Conclusion

For the study of the behavior of the oscillating superleak transducers, summarized in the previous chapters, the focus was set on three major topics:

1. Noise Suppression
2. Distance Variation
3. Frequency Analysis

Each of them contributed to a better understanding of the examined device.

Different experiences were gained in the field of **noise suppression**, especially as the measurements were done at two setups under different circumstances. At Göttingen, the stopping of the vacuum pump and the shielding were responsible for the biggest improvements. In the Cryolab at CERN, the local ground connection was the major cause for unwanted frequencies. For both setups, switching to a battery driven power supply of the senors resulted in a smaller noise background. These experiences are very fundamental, although probably true for any similar experiments with electrical signal transmission. Nevertheless, it is very important to keep them in mind for any future setups, as they — such as in the case of the SPL test cavity — might be much more complex in their structure.

The experiments with a **variation in the distance** between heat source and sensor were done with the intention to prove that this particular method of distance determination works properly. Although the precision itself achieved with the data of the experiments at Göttingen is in the order of a few centimeters, it has been shown that the recorded signal follow the principle of the prediction. The results of the measurements at the Cryolab, which are in the order of a few millimeters, confirm this conclusion. From the qualitative point of view, the increase of the distance has caused an elongation of the time of flight at both setups. Furthermore, the very start of the signal is in agreement with the theory of the working principle of the OSTs as it reflects the decrease of the gap between the capacitor plates with a negative peak in the voltage. This understanding was again verified in the experiments with polished and non-polished electrodes. The decrease in the average distance between the gold layer and the brass electrode causes a

gain in the amplitudes of the voltage change. With the used method, an improvement of a factor of two and more could be achieved for the used devices.

In order to prepare an automation of the distance determination, an algorithm for an amplitude threshold scan of the signals has been developed. The evaluation of the Göttingen measurements with this program unveil a non-constant delay in the signal start, the biggest amplitudes take time to build up. This effect has already been seen in the qualitative comparison of the recorded curves and the predicted signal start interval as shown in figure 4.6. The outcome of the same evaluation performed for the experiments of the Cryolab at CERN is much different from that. The distance or respectively time deviation from the prediction is much smaller. The successful noise suppression and the used amplifier circuit result in a distance error which is smaller than 3 mm for most distances, compare figure 5.5.[1]

Additionally, the behavior of the deviation with increasing distance shows strong similarities with the coverage of the opening angle above the heater by the membrane, compare figure 4.7. One reason for this might be the transition of the second sound wave from a spherical to a planar wave propagation as seen from the point of view of the OST. This correlation has already been noticed in the change of the amplitudes for different distances in the Göttingen data. It impedes the precise distance determination for very small distances in the order of the membranes own dimensions. In a setup for a heat source localization on the surface of an elliptical sc rf cavity, the minimal spatial displacement of the OSTs from the surface should therefore be larger than this.

The results of the **frequency analysis** are very different for the two described setups. The OST used in Göttingen responds to the second sound wave with frequencies in the order of 300, 550 and 850 Hz. The two latter ones are probably higher order modes of the 300 Hz as discussed in [33]. After the final noise reduction, all three frequencies are still ubiquitous in all recorded signals. Hence, an origin in the noise background can be excluded. In contrast to that, the OST responses at the Cryolab at CERN show a wider frequency variation in the single digit kHz regime for all — CERN, DESY and Cornell built — devices. The frequencies observed in Göttingen do not appear in their spectrum. The analysis and comparison among the different devices does instead emphasize that the response frequency is an individual characteristic of the mechanical structure. The tightening of the screws fixation, which has been more or less arbitrary, might have an impact on this behavior. There are other strong hints that the transducers keep their own frequency for several cooling cycles as long as they are not disassembled. However, this theory demands further investigations. Using the individual characteristic frequencies, a threshold scan algorithm, similar to the one developed for the signal's amplitude, has been developed for the Fourier space. The deviation for the distance determination is larger than for the amplitude approach, but still less than 6 mm for distances of up to 22 cm. The reason for this lies in the nature of the method itself. While the amplitude scan searches for a rising or falling slope in the signal, the frequency scan needs an

[1] As mentioned earlier, this agrees with the estimation of [32], so that the resolution of less than 5 mm for the quench spot localization, which has been computed for a nine-cell TESLA cavity, might be possible with these results.

extended part of the wave to extract the dominant frequency, compare figure 5.7. A combination of both methods for an automated signal analysis should be useful, especially as the frequency scan helps to resolve signals with a high noise background.

The lower frequency results of the sensor used at Göttingen are stable but not verified in terms of crosschecks. Only one unique OST has been used for all the measurements at the same setup. It is hard to tell if the device's own properties or also the special geometry of the cryostat influenced the outcome. For a sophisticated study, other detectors have to be tested at this setup. As an alternative, the used OST itself could be tested in a different setup like the one at the Cryolab.

Besides the recording and processing of the second sound signals at smaller cryostats, further expertise for the application was gained during the preparation of the SPL prototype cavity measurement. The setup itself, including the read out chain, has been prepared. Additionally, all installed OSTs were produced, assembled and tested at CERN.

Chapter 8.

Outlook

The work, presented in this thesis, has yielded several interesting and useful results for the application of second sound sensitive OSTs. Some recommendations can be deduced within the framework of this outlook:

As the amplitude of the voltage change in the signals of the OSTs was used to determine the time of flight of the second sound wave, it is of great importance to separate it from the noise background. It has been shown on the hardware side of the sensor, that a reduction of the distance between the two capacitor plates can be obtained by polishing the brass electrode. Because of the significant gain in the capacity and voltage change achieved with this method, it is planned to polish all used OSTs at CERN in the near future. Furthermore, the measurements at different temperatures of the liquid helium pointed out, that the signal to noise ratio suffers for higher temperatures, compare figure 5.9. It is therefore recommended to keep the helium bath temperature below at least 1.8 K to acquire sufficient amplitudes in the signal. Finally, as mentioned in the conclusion, the affiliation of the amplitude and the frequency thresholds is very useful for future automated heat source localizations.

Summarizing the future projects, the distinction between small setups in a cryostat and cavity measurements is suggested. The setups at Göttingen and at the Cryolab at CERN are suitable for calibration purposes. Therefore, other research facilities, for instance the KEK in Japan and the CEA at Saclay in France, have been planning to set up similar experiments. At cryostats of this kind, all produced sensors can be studied. Their characteristic frequencies can be determined and used to adjust the corresponding threshold scans. At CERN itself, measurements of second sound reflections in a niobium tube are planned to be done in the near future.

In the field of cavity measurements, the SPL prototype test at the experimental hall SM18 is the very next step in the efforts at CERN. As soon as the first results come in, the created software solutions and expertise can be adapted and used to process them. After that, more tests — at some point also for five-cell structures — are pending. Additionally to these second sound tests, a system for an optical inspection of the inner surface of the cavities and a temperature mapping system are currently under development. Just like for the ongoing projects for the TESLA cavities at DESY, these diagnosis methods may be combined in the future.

Acknowledgments

Many people have been involved in the work presented in this thesis. They all contributed in their very own way. It is hard to bring them all up and I want to apologize in advance to everyone I might forget to mention here. I would like to go through the list of people who I owe a lot of thanks in the inverse order, so starting with the ones at CERN:

First of all, I want to thank Didier Glaude from the metrology section, who made it possible to conduct a fast but sophisticated surface measurement of our electrodes. Furthermore, I would like to thank Christophe Nicou, Antoine Lopez, Luca Arnaudon and all the other people in the workshops at CERN, who not only made it possible to manufacture our own sensors, but also helped to solve a lot of other problems concerning our electronics. I kindly thank Wilhelmus Vollenberg for the sputtering of our membranes. At the Cryolab, I would like to express my gratitude to Johan Bremer, Christoph Balle, Sebastian Prunet and Laetitia Dufay-Chanat for their readiness to help us at any time. Special thanks go out to Thomas Eisel and Thomas Forgber who have done an incredible job to realize my and my colleague's visions for our setup.

A lot of people in my section contributed to the success of our project. I would like to mention Olivier Brunner, Janic Chambrillon, Pierre Maesen and Matthieu Therasse. I have to emphasize the huge impact of my colleague Tobias Junginger, he has been an ideal example of a PhD student guiding younger scientists where ever he could, although it does not reduce his very own workload at all. My very special thanks go out to my closest associate Kitty Liao and my supervisor Wolfgang Weingarten, who have started the whole second sound project at CERN together with Tobias. I wish them great success for their future work, not only in this particular field. Finally, I have to add that I am deeply grateful for the warmest welcome and introduction to not only the section but the whole of CERN I have received from everyone but especially Nikolai Schwerg. In summary, all these people made me enjoy my stay at CERN, they have taught me a lot and improved many of my abilities and virtues — I guess especially my interest in science and patience with the same.

At Göttingen, I first of all want to thank Arnulf Quadt, the head of the 2nd Institute of Physics, who has made this whole project possible in the first place and who has never stopped to raise motivation and dedication to it. In addition to him, I would like to thank the people of the local hardware meeting, especially Jörn Große-Knetter and Jens Weingarten, who have given a lot of input to our experiments. Furthermore, the people at the local workshops shall be thanked as well for all their help. Eventually there is my own group which I like to thank: Benjamin Schröder has worked with me for almost a year since he started with his Bachelor thesis and Benjamin Willenberg has joined

us recently this summer. Finally, the head of our group, Michael Uhrmacher, deserves my biggest thanks, as he has supervised me since 2009 and had to stand my annoying questions and comments during this time — he did an outstanding job. I wish him and Wolfgang Weingarten from CERN all the best for their retirement!

Beside these acknowledgments for the people in my professional life, I bear the strong believe, that my parents and my brother are aware of my unlimited gratitude for their love and support throughout these years.

Appendix

Additional Figures and Pictures

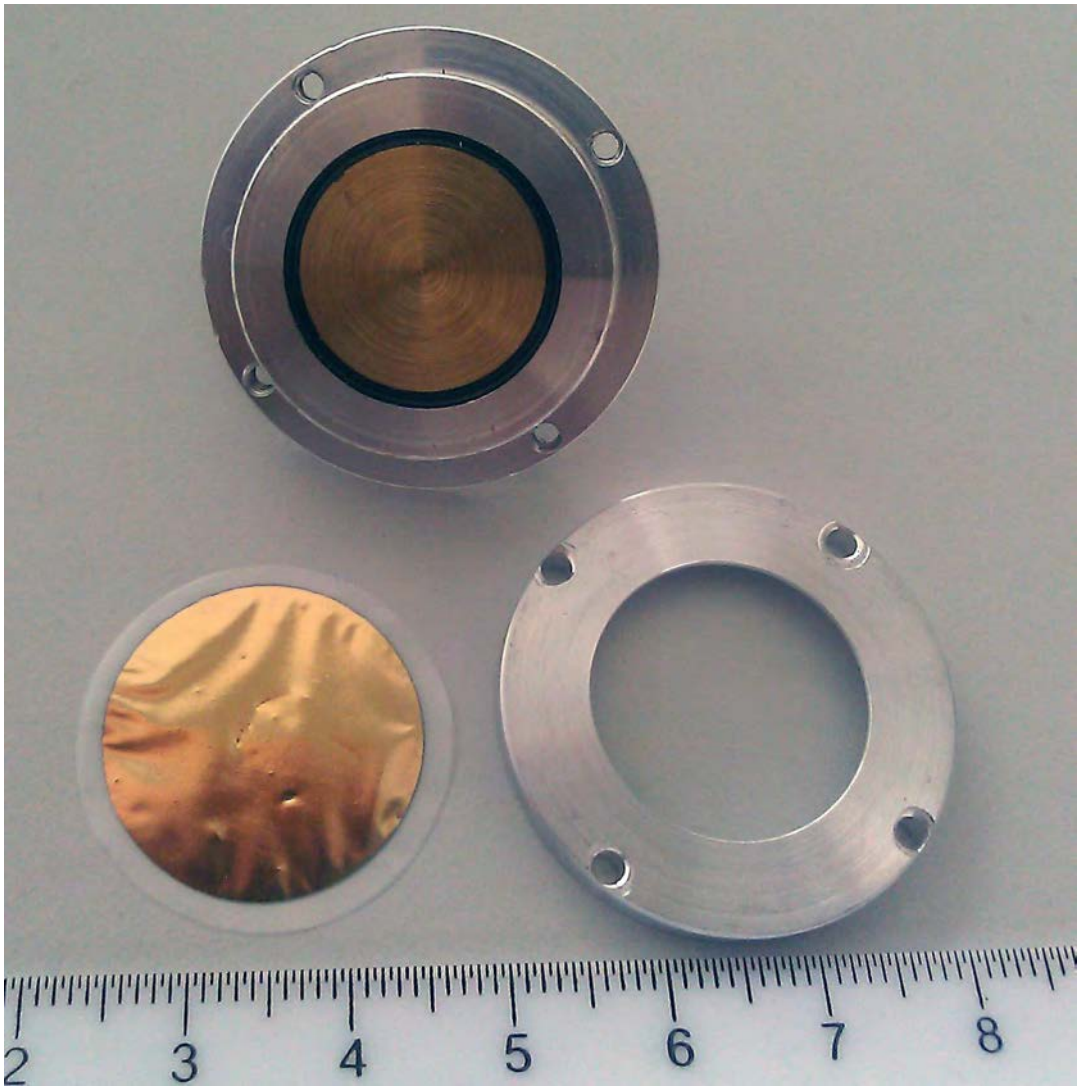

Figure 9.1.: Picture of an disassembled OST build at CERN: The brass electrode is glued in the back of the casing, the scale is in cm.

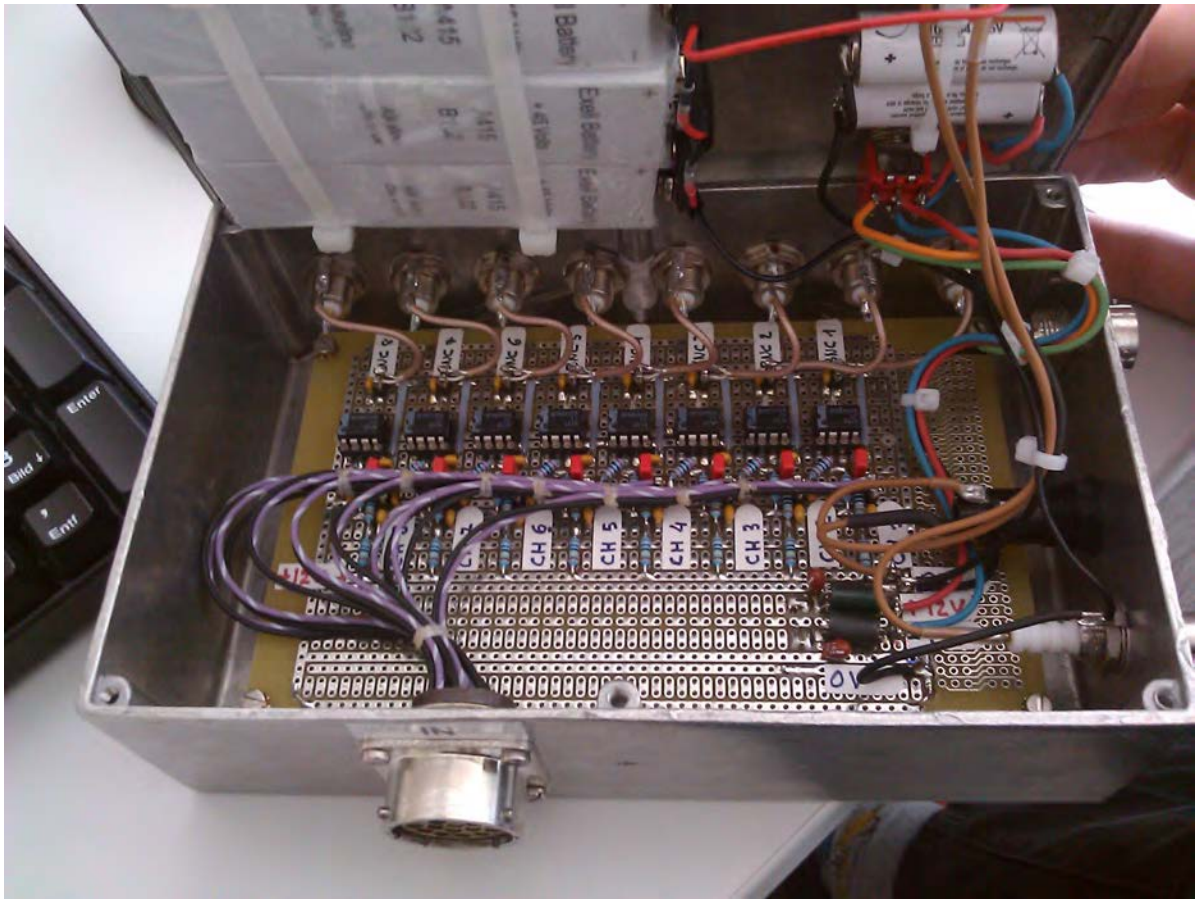

Figure 9.2.: Picture of the open amplifier box containing eight read-out channels and their amplification cicuits as well as the batteries for their power supply, fixed under the cover of the metallic box.

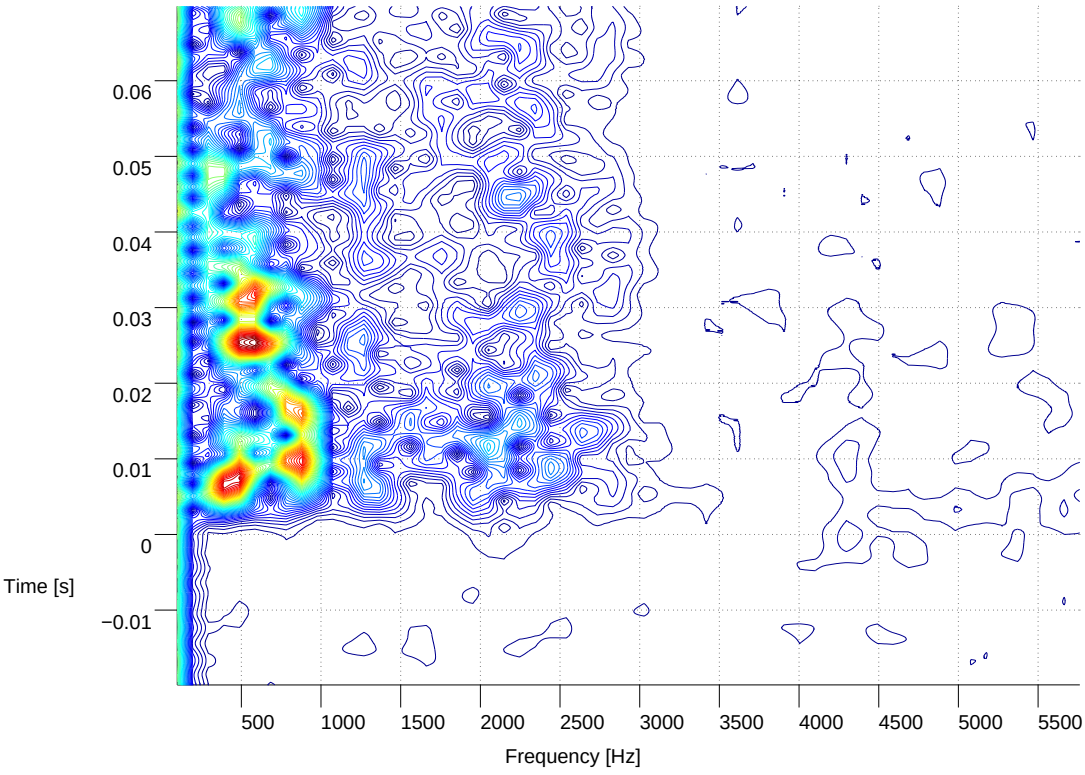

Figure 9.3.: Contour map of the evolution of the Fourier spectrum per time interval of 1 ms of a second sound signal measured in Göttingen.

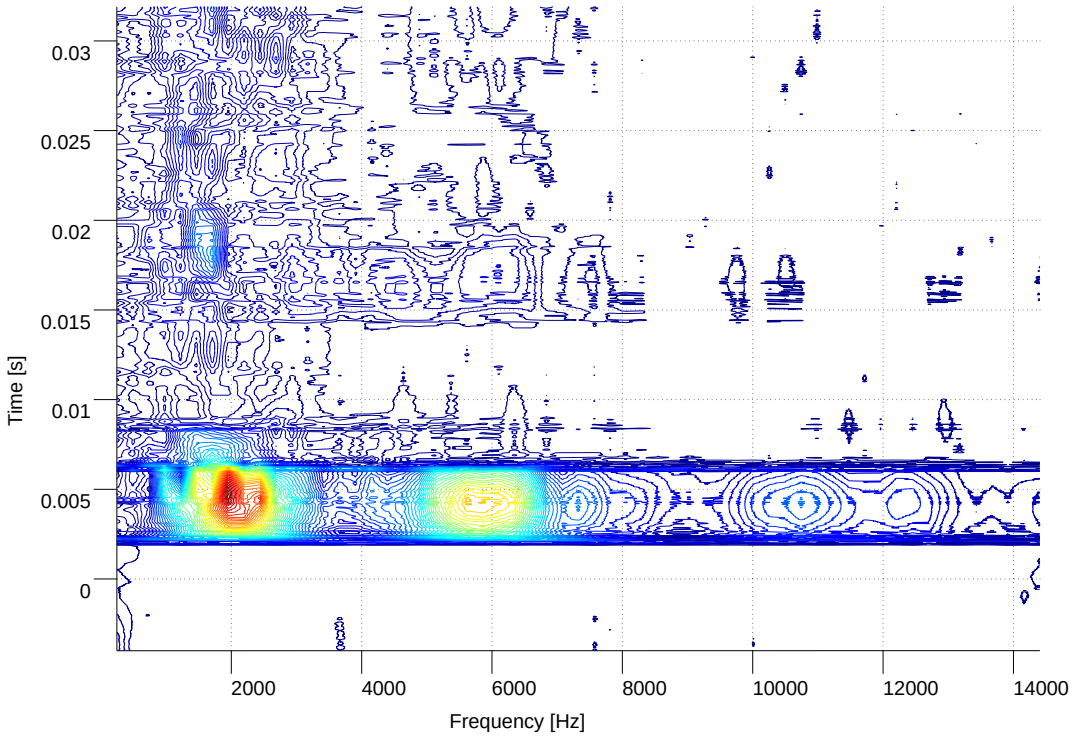

Figure 9.4.: Contour map of the evolution of the Fourier spectrum per time interval of 4 ms of a second sound signal measured in the Cryolab at CERN.

Figure 9.5.: Picture of the insulating element in the metal pump line.

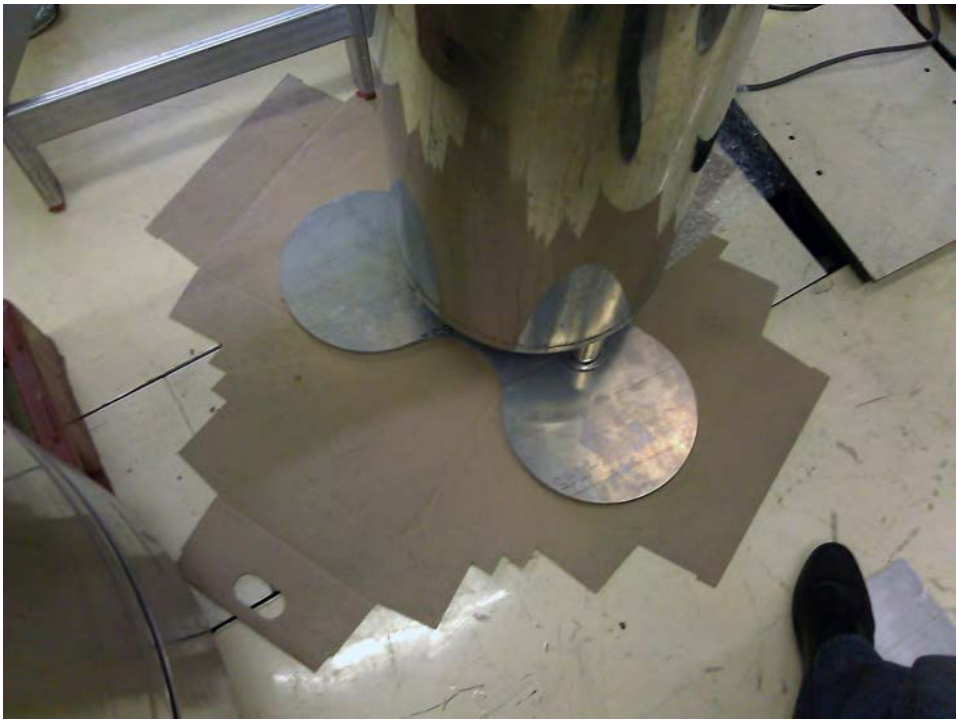

Figure 9.6.: Two cardboard layers as an insulation from the conducting floor.

Figure 9.7.: Picture of the work desk with several OST components at the workshop at CERN.

Figure 9.8.: Picture of the injection of the liquid glue under the electrode.

Figure 9.9.: Picture of the glue spreading process via lowering the electrode in the casing.

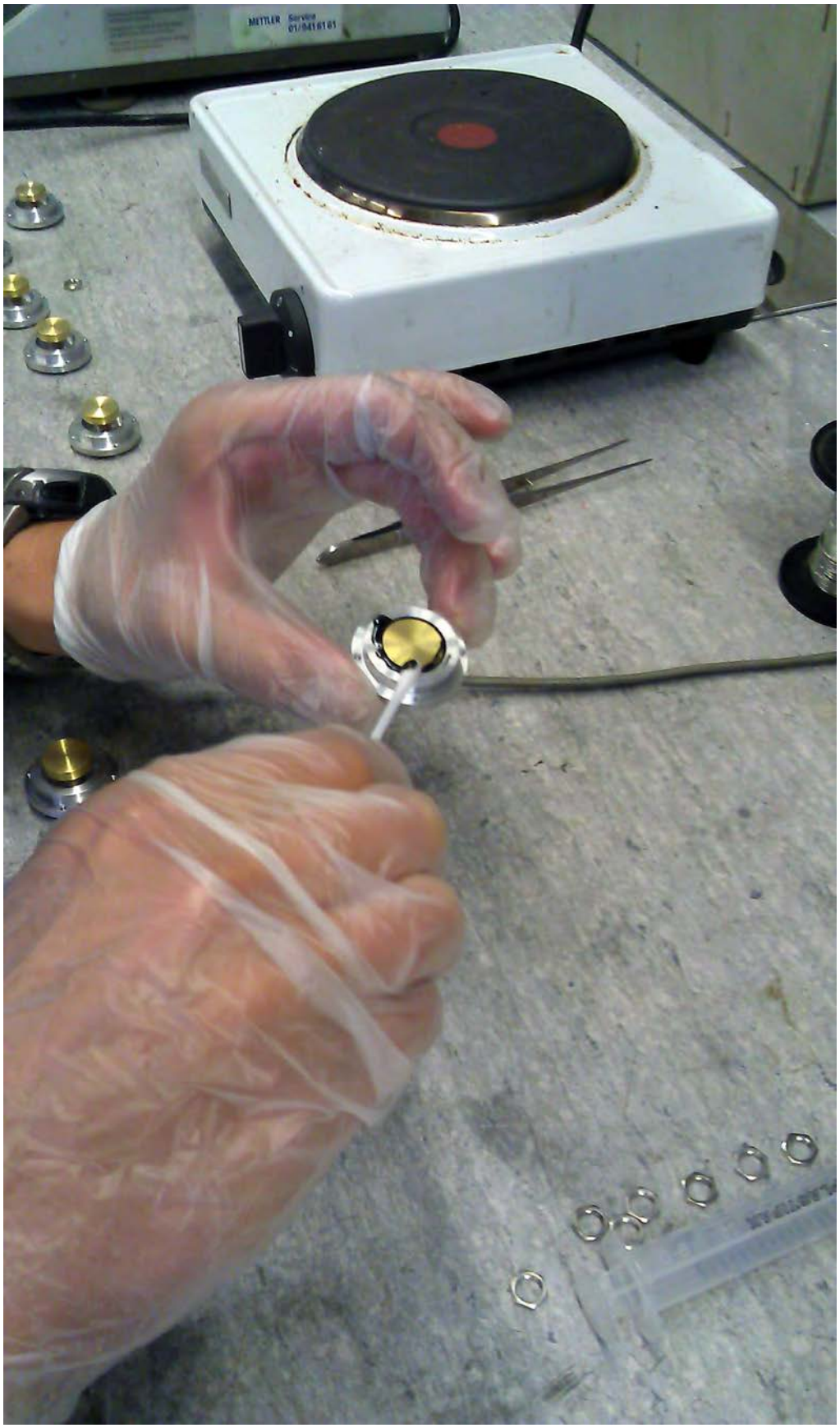

Figure 9.10.: Picture of the final cleaning of the back part of the OSTs casing.

Figure 9.11.: Picture of a fully assembled OST with its holder for the SPL test setup.

Figure 9.12.: Picture of two OST electrodes in their casings, on the left a CERN built one, on the right the version from Cornell University.

Figure 9.13.: Picture of two installed OST plugs, on the left the LEMO series 00 used at CERN, on the right the SMA used at Cornell University and DESY.

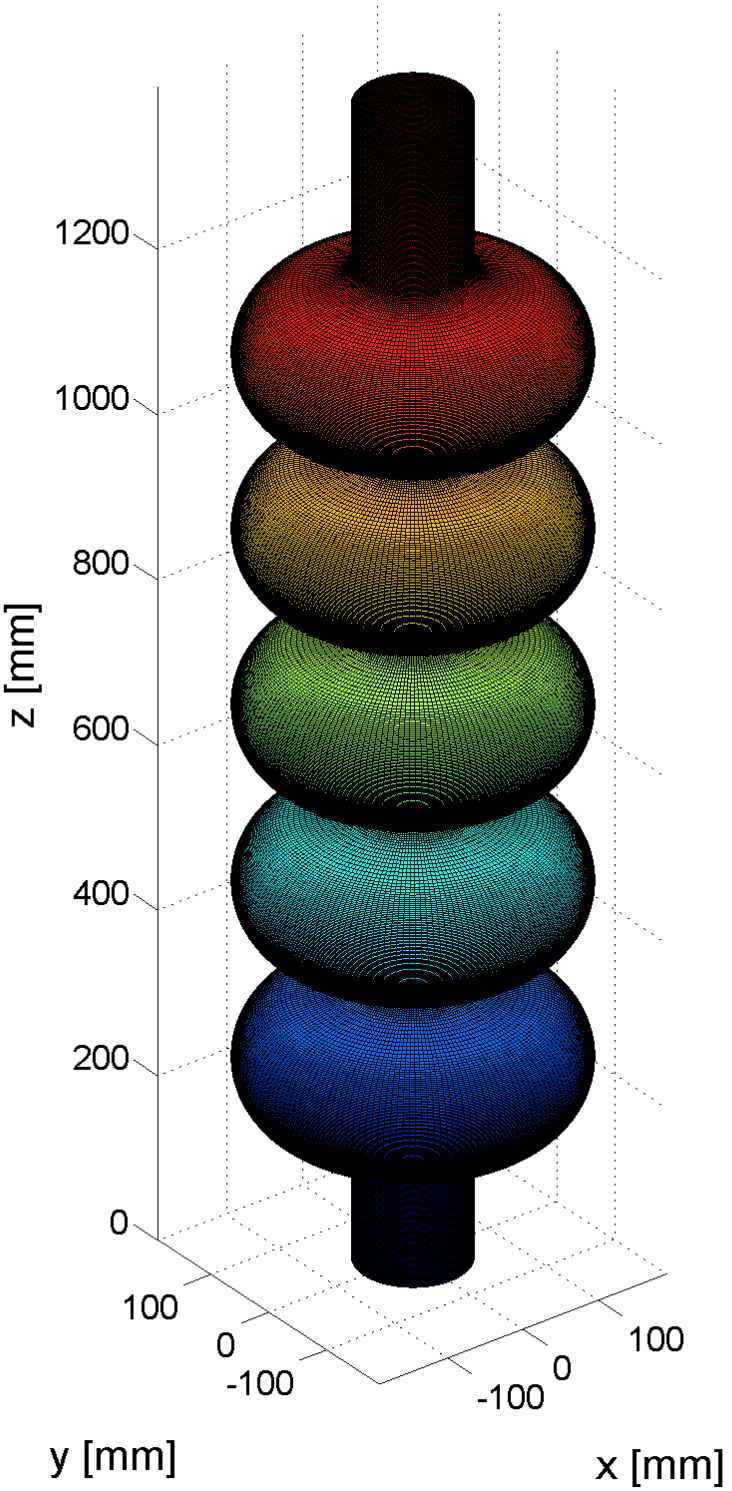

Figure 9.14.: Matlab figure of the SPL five-cell structure surface.

Bibliography

[1] J. Sagendorf. Optical Inspection of SRF Cavity Defects. 2010.

[2] A. Djouadi et al., editor. *International Linear Collider Reference Design Report*, volume 2: Physics at the ILC. International Linear Collider Collaboration, 2007.

[3] N. Phinney, N. Toge, N. Walker, editor. *International Linear Collider Reference Design Report*, volume 3: Accelerator. International Linear Collider Collaboration, 2007.

[4] Massimo Altarelli et al, editor. *European XFEL - Technical Design Report*. DESY XFEL Project Group European XFEL Project Team, 2007.

[5] R. Garoby. Status and Plans of the SPL Study at CERN. Technical report, SPL Study Group CERN, 2002.

[6] O. Capatina et al. Mechanical design considerations for beta=1 cavities. In *SRF Conference 2011*, 2011.

[7] O. Brunner et al. Assessment of the basic parameters of the CERN Superconducting Proton Linac. *Phys. Rev. ST Accel. Beams*, 12:070402, 2009.

[8] R. Garoby et al. Conceptual Design of the SPL, a high-power superconducting H^- Linac at CERN. Technical report, CERN, 2000.

[9] G. Olry. SPL Cavity Development. In *SRF Conference 2011*, 2011.

[10] C. P. Poole et al. *Superconductivity*. Elsevier, second edition, 2007.

[11] J. Knobloch, T. Hays, H. Padamsee. *RF Superconductivity for Accelerators*. Wiley-VCH, second edition, 2008.

[12] W. Buckel, R. Kleiner. *Superconductivity: Fundamentals and Applications*. WILEY-VCH, second edition, 2004.

[13] H. Padamsee. *RF Superconductivitiy*. Wiley-VCH, first edition, 2009.

[14] R.L. Geng, editor. *High gradient sudies for ILC with single-cell re-entrant shape and elliptical shape cavities made of fine-grain and large-grain Niobium*, volume WEPMS006, 2007.

[15] A. Yamamoto. Advances in SRF Development for ILC. In *SRF Conference 2011*, 2011.

[16] D. Reschke, editor. *Analysis of Quenches using Temperature Mapping in* 1.3 GHz *SCRF Cavities at DESY*. DESY, 2008. Proceedings of LINAC08.

[17] O. Chodosh, J. Hiatt, S. Shah, N. Yan. Second Sound in Helium II. March, 2008.

[18] R. J. Donnelly. The two-fluid theory and second sound in liquid helium. *Physics Today*, 10:34–39, 2009.

[19] Z. Conway, D. Hartill, H. Padamsee. Oscillating Superleak Transducers for Quench Detection in superconducting ILC Cavities cooled with He-II. *TTC-Report*, 06, 2008.

[20] K. W. Shepard et al. Split Ring Resonator for the Argonna Superconducting heavy Ion Booster. *IEEE Transactions on Nuclear Science*, 3, 1977.

[21] B. Schröder. Experiments on second sound using OST and heat spot. University of Göttingen – II.Physik-UniGö-Bach2010/08, 2010.

[22] H. Vennekate. Single OST Second Sound Measurements in a Glass Cryostat. University of Göttingen, March 2011.

[23] University of Göttingen. *I. Physikalisches Institut: Anleitung zum Versuch F2*, November 2009.

[24] Leybold Vacuum. *Product Information – IONIVAC Transmitters ITR 90*.

[25] *MSO4000B and DPO4000B Series Digital Phosphor Oscilloscopes User Manual*. Tektronix, Inc.

[26] Lake Shore Cryotronics, Inc. *Calibration Report: 633011, Cernox CX-1050-SD-1.4L*.

[27] K. Krizka. Summary of Testing Oscillating Superleak Transducers at CERN.

`www.ipp.ca/pdfs/krizka_report.pdf`

last visited December 12$^{\text{th}}$, 2010.

[28] R. Kories, H. Schmidt-Walter. *Taschenbuch der Elektrotechnik*. Verlag Harri Deutsch, 8 edition, 2008.

[29] *TDS3000C Series Digital Phosphor Oscilloscopes User Manual*. Tektronix, Inc.

[30] *MSO3000 and DPO3000 Series Digital Phosphor Oscilloscopes User Manual*. Tektronix, Inc.

[31] R. T. Wang, W. T. Wagner, R. J. Donnelly. Precision Second-Sound Velocity Measurements in Helium II. *J. Low Temp. Phys*, 68:409–417, 1987.

[32] H. Vennekate. Second Sound as Cavity Diagnostic Tool. University of Göttingen – II.Physik-UniGö-Bach2009/04, 2009.

[33] B. Willenberg. On the Response of an OST to Second Sound. University of Göttingen – II.Physik-UniGö-BSc-2011/03, 2011.

[34] J. W. Cooley, J. W. Tukey. An algorithm for the machine calculation of complex Fourier series. *Math. Comput*, 19:297–301, 1965.

[35] Thermal Expansion of Technical Solids at Low Temperatures. National Bureau of Standards. A Compilation from the literature, NBS Monograph 29.

[36] R. A. Sherlock, D.O. Edwards. Oscillating Superleak Second Sound Transducers. *The Review of Scientific Instruments*, 41:1603–1609, 1970.

[37] F. Schlander, H. Vennekate. Investigations on Improvements of Oscillating Superleak Transducers. Technical report, ILC HiGrade, August 2011.

[38] Wyko NT3300 Optical 3d Profiling System. Veeco Instruments Inc. NT3-4-0201, 2001.